nature chemical biology

Article

https://doi.org/10.1038/s41589-024-01559-8

Antiviral drug recognition and elevator-type transport motions of CNT3

Received: 1 September 2023

Accepted: 22 January 2024

Published online: 28 February 2024

Check for updates

Nicholas J. Wright[1], Feng Zhang[1], Yang Suo[1], Lingyang Kong[2], Ying Yin[1], Justin G. Fedor[1], Kedar Sharma[3], Mario J. Borgnia[3], Wonpil Im[2] & Seok-Yong Lee[1]

Nucleoside analogs have broad clinical utility as antiviral drugs. Key to their systemic distribution and cellular entry are human nucleoside transporters. Here, we establish that the human concentrative nucleoside transporter 3 (CNT3) interacts with antiviral drugs used in the treatment of coronavirus infections. We report high-resolution single-particle cryo-electron microscopy structures of bovine CNT3 complexed with antiviral nucleosides N^4-hydroxycytidine, PSI-6206, GS-441524 and ribavirin, all in inward-facing states. Notably, we found that the orally bioavailable antiviral molnupiravir arrests CNT3 in four distinct conformations, allowing us to capture cryo-electron microscopy structures of drug-loaded outward-facing and drug-loaded intermediate states. Our studies uncover the conformational trajectory of CNT3 during membrane transport of a nucleoside analog antiviral drug, yield new insights into the role of interactions between the transport and the scaffold domains in elevator-like domain movements during drug translocation, and provide insights into the design of nucleoside analog antiviral prodrugs with improved oral bioavailability.

There is a dire need for improved small-molecule therapeutics to treat viral diseases. Nucleoside analog antivirals (NAAs) represent a large class of drugs against a variety of infectious agents, including hepatitis C virus (HCV), severe acute respiratory syndrome coronavirus 2 (SARS-CoV-2) and influenza viruses[1,2]. The mechanisms of action include inhibition of viral replication through polymerase inhibition, lethal mutagenesis and nucleic acid chain termination[1–4]. NAA drugs are prodrugs, meaning that they require cellular uptake and subsequent phosphorylation to transform into their active nucleotide triphosphate form.

The efficacy of NAAs relies on their systemic distribution and disposition. Remdesivir (a Food and Drug Administration (FDA)-approved therapeutic for SARS-CoV-2)[5], sofosbuvir (an FDA-approved therapeutic for HCV)[6] and molnupiravir (MPV; currently under FDA Emergency Use Authorization for SARS-CoV-2)[7] harbor protecting groups (PGs) at the 5′ position of their parent nucleosides GS-441524 (GS4), PSI-6206 and N^4-hydroxycytidine (NHC; Supplementary Fig. 1). Pharmacokinetics studies showed that serum esterases and phosphoramidases rapidly convert these drugs into the parent nucleoside forms, rendering them the dominant species in plasma[8–12]. In some cases, PGs are not required for optimal efficacy, as ribavirin (Supplementary Fig. 1) is an unprotected NAA with a rich history of clinical use against HCV[4,13], GS4 has proven activity against feline coronavirus infection in vivo[14], and NHC is a broad-spectrum antiviral against various viruses including coronaviruses[10,15] and influenza viruses[16,17]. There is a growing demand for rigorous testing of unprotected NAAs to assess their clinical potential[11].

Regardless of 5′-hydroxyl PGs (5′-PGs), free NAAs are systemically distributed shortly after drug administration[8–11]. These xenobiotics are small hydrophilic molecules that depend on two distinct carrier families for NAA membrane transport in humans: concentrative nucleoside transporters (hCNTs) of the solute carrier (SLC) family 28 (refs. 18–21) and equilibrative nucleoside transporters (hENTs) of the SLC family

[1]Department of Biochemistry, Duke University School of Medicine, Durham, NC, USA. [2]Departments of Biological Sciences, Chemistry, and Bioengineering, Lehigh University, Bethlehem, PA, USA. [3]Department of Health and Human Services, Genome Integrity and Structural Biology Laboratory, National Institute of Environmental Health Sciences, National Institutes of Health, Research Triangle Park, Durham, NC, USA.
e-mail: seok-yong.lee@duke.edu

29 (refs. 22–24). Both hCNTs and hENTs play crucial roles in the pharmacokinetics and pharmacodynamics of NAAs, as they control NAA distribution and cellular entry into infected cells. This is supported by reported correlations between human nucleoside transporter expression levels or polymorphisms and responsiveness to NAAs, ribavirin being a prime example[25–29]. Recent reports highlight the role of human nucleoside transporters in SARS-CoV-2 therapeutic action[30].

hCNT subtype 3 (hCNT3), a sodium-coupled nucleoside symporter, is the most effective human transporter for cellular GS4 uptake[31], consistent with its role in a broad range of NAA transport[32]. hCNT3 exhibits high expression in epithelial cells[22], wide substrate specificity and a 2:1 sodium:nucleoside coupling stoichiometry, which contrasts the narrow nucleoside selectivity and 1:1 coupling ratios in subtypes 1 and 2 (ref. 33). Therefore, understanding the nature of drug interactions with hCNT3 will prove critical for developing therapeutics with improved pharmacological properties.

There is a wealth of previous structural studies concerning the nucleoside recognition and elevator alternating access mechanisms by the CNT family, but they are mostly limited to bacterial CNTs[18–21]. Our understanding of antiviral drug recognition and transport by mammalian CNTs is relatively incomplete, with numerous questions remaining. Are NAA prodrugs efficiently translocated by mammalian CNT3? Does the conformational trajectory of drug-loaded carrier during translocation deviate from what is reported for the apo-carrier? Do the subunits of the CNT3 trimer operate independently? Or do they exhibit any cooperativity? Here, we address these open questions and delve into the mechanisms of NAA recognition and transport by a mammalian CNT3. We discovered that the prodrug MPV exhibits severely altered transport properties compared to its parent NAA NHC, elucidated cryo-electron microscopy (cryo-EM) structures of numerous distinct MPV-arrested CNT3 conformations, interrogated the energetic landscape of NAA translocation via CNT3 and explored the structural basis of subunit cooperativity between subunits within a CNT3 trimer. Our findings also present an idea that could be useful in the design of NAA prodrugs with improved pharmacological properties.

Results

Antiviral drug interaction at hCNT3

We expressed five human nucleoside transporter subtypes in *Xenopus laevis* oocytes (Extended Data Fig. 1a–c) and assessed the ability of cold NHC or GS4 to competitively inhibit [^{3}H]nucleoside uptake. Both antiviral nucleosides substantially inhibited [^{3}H]ribavirin uptake at hCNT1–hCNT3 and hENT1 (Fig. 1a). NHC and GS4 showed half-maximal inhibitory concentration (IC_{50}) values of ~13 µM and ~400 µM, respectively, for hCNT3-mediated [^{3}H]ribavirin uptake (Fig. 1b). Unexpectedly, the prodrug MPV also showed an IC_{50} value of ~55 µM (Fig. 1b). These results confirm drug interactions with these human nucleoside transporter subtypes, but their transportability remains ambiguous. Because CNTs are sodium-coupled symporters, cotransport of nucleoside and sodium ions is electrogenic, which can be measured with two-electrode voltage-clamp (TEVC)[33]. Using TEVC, we found that NHC evokes inward sodium currents in oocytes expressing hCNT3 to levels similar to uridine, suggesting that it is a substrate for hCNT3 (Fig. 1c). Regarding GS4, because hCNT3 raw functional activity was lower in radiotracer uptake experiments either due to weaker surface expression or lower turnover rate (Extended Data Fig. 1d), we used *Bos taurus* CNT3 (bCNT3) to detect GS4-evoked inward sodium currents and found that GS4 is a substrate for bCNT3 (Fig. 1d). In line with this, GS4 was reported to be transported by hCNT3 (ref. 31).

Structure determination and transporter architecture

The bCNT3 ortholog exhibits excellent biochemical stability in detergent buffer. bCNT3 is 79% identical to hCNT3, with the residues corresponding to nucleoside coordination[19,20] absolutely conserved between the orthologs (Supplementary Fig. 2). Functionally, bCNT3 mediates sodium-dependent uptake of [^{3}H]ribavirin when expressed in oocytes, with its uptake activity inhibited by the presence of cold NHC or GS4 (Extended Data Fig. 1d). We first obtained six cryo-EM reconstructions of bCNT3 in lipid nanodiscs, including drug-free and drug-bound states (NHC, GS4, PSI-6206 and ribavirin), in the presence of NaCl (Fig. 2, Extended Data Figs. 2 and 3 and Supplementary Table 1). The reconstructions are of high quality, ranging in resolution from 2.31 Å to 3.23 Å, and feature layers of lipid densities (Fig. 2a and Extended Data Figs. 2 and 3).

For consistency with previous CNT studies[18–20], we preserve the numbering for conserved structural elements. The architecture is divided into two parts, a (1) 'scaffold domain', which serves as a rigid trimerization interface that also surrounds the mobile (2) 'transport domain' (Supplementary Fig. 3a,b). In the scaffold domain, transmembrane helices 3 and 6 (TM3 and TM6) participate in the trimerization, and TM6 serves as a hydrophobic barrier to nucleoside transport (Supplementary Fig. 3a,b)[18,20]. The nucleoside binding site is in the transport domain at the interface of TM4b, TM7b, helical hairpin 1 (HP1) and HP2. A feature unique to eukaryotic CNTs is three additional TMs (denoted $TM1^{Eu}$–$TM3^{Eu}$) and two interfacial helices ($IH1^{Eu}$–$IH2^{Eu}$) at their N termini[21], which we term the 'eukaryotic scaffold domain' (Supplementary Fig. 3a,b). Part of this motif is domain swapped, where $IH1^{Eu}$ and $TM1^{Eu}$ contact the neighboring protomer. Well-ordered lipids occupy the crevices between the eukaryotic scaffold and transport domains (Fig. 2a). Deletion of this eukaryotic scaffold domain reduces transport activity by 94–97% but does not abolish function[34]. This domain has also been implicated in membrane trafficking and protein–protein interaction[35].

Antiviral drug recognition in the IFS

All six aforementioned cryo-EM structures adopt nearly identical conformations with global Cα root mean squared deviation (r.m.s.d.) values of ~0.2 Å within the protomer (Extended Data Fig. 2). Considering that the nucleoside binding pockets are below TM6 and open to the intracellular solution, they represent inward-facing states (IFSs; Supplementary Fig. 3a,b). This apparent propensity for bCNT3 adopting the IFS after detergent extraction, in the presence of NaCl, is consistent with previous structural studies of CNTs[18–21]. The quality of the maps enabled unambiguous modeling of nucleoside drugs for NHC, PSI-6206 and ribavirin, including the assignments of the nucleobase ring orientation and the sugar pucker of ribose as 3′-endo ('north'), consistent with previous studies on CNTs (Fig. 2b, Supplementary Figs. 3–5 and Supplementary Table 2)[19,36]. Although GS4 is a low-affinity CNT3 substrate (Fig. 1a,b) and the initial reconstruction showed no clear drug density ('GS4 consensus'; Fig. 2b), after extensive image classification (Extended Data Fig. 2) a subset of particles yielded a reconstruction with a noticeable drug density, enabling GS4 modeling ('GS4 subset'; Fig. 2b).

The poses for all four drugs are similar, as side chains of HP1 and TM4 interact with the nucleobase portion of the drug, whereas those of HP2 and TM7 interact with the ribose portion of the drug (Fig. 2b). Central to ligand binding is F569, in an unwound portion of TM7, that forms a π–π interaction with the nucleobase ring[18–20]. NHC is a cytidine analog, with the only difference being an N^4-hydroxyl group. This substituent interacts with S380 in the bCNT3–NHC structure and likely contributes to its high affinity for CNT3 (Fig. 1a–c and Extended Data Fig. 1d). The anti-HCV nucleoside PSI-6206 is a uridine analog and features a fluorine at the epimeric position analogous to the 2′-hydroxyl group and a methyl group at the opposite epimeric position at 2′ of its ribose. This 2′ methyl substituent appears to alter the drug's interaction with TM7, as it pushes the ribose moiety away from TM7 and F569 (Supplementary Fig. 3c,e). The broad-spectrum NAA GS4 features a cyano group at the 1′ position at the epimeric position

https://doi.org/10.1038/s41589-024-01559-8

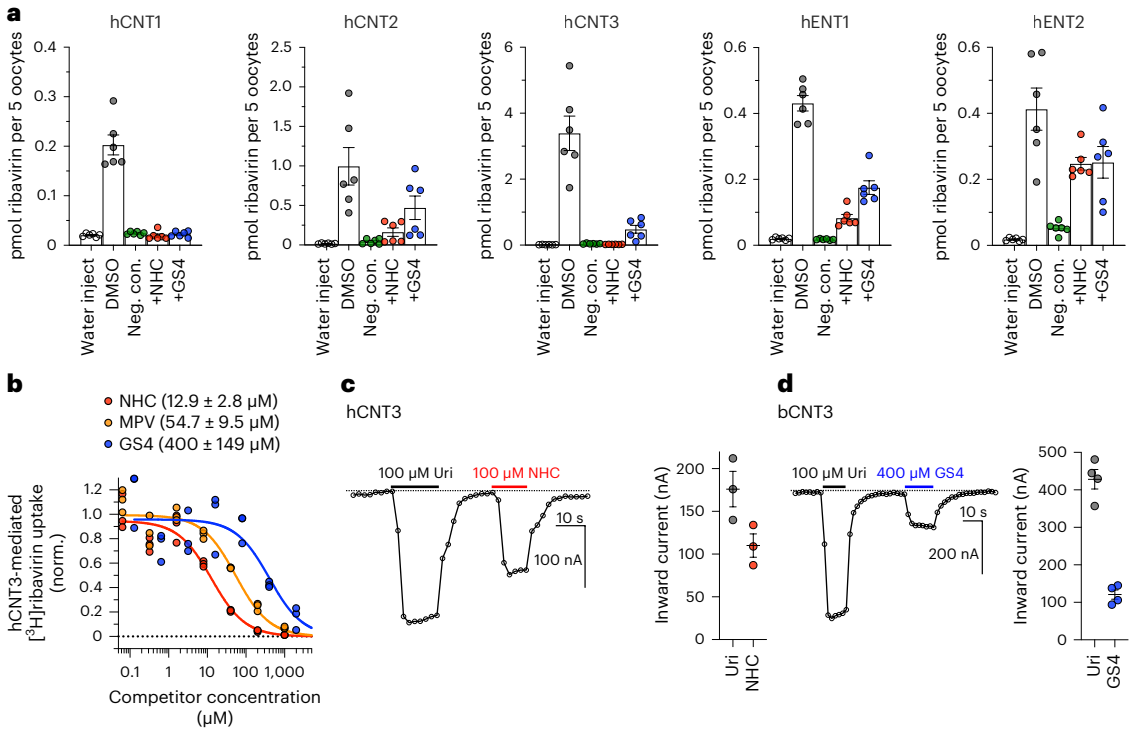

Fig. 1 | NAAs interact with hCNT3. a, Cold competition of 1.0 mM unlabeled NHC or GS4 against 1.0 μM [^{3}H]ribavirin uptake mediated by nucleoside transporter-expressing *X. laevis* oocytes in 5 min (wild-type (WT) hCNT2, WT hCNT3, WT hENT1 and WT hENT2) or 15 min (WT hCNT1). The following negative controls were used: sodium-free ND-96 (96 mM choline chloride) medium for all hCNT isoforms, +10 μM dilazep (ENT-specific inhibitor) for hENT1 and +1.0 mM dilazep for hENT2 ($n = 6$ biological replicates; individual replicates and mean ± s.e.m. are shown); Neg. con., negative control. **b**, Cold competition inhibition of WT hCNT3-mediated [^{3}H]ribavirin uptake by NHC, GS4 or MPV (15-min uptake with 1.0 μM [^{3}H]ribavirin and coapplied cold inhibitor; $n = 3$ biological replicates with individual replicates shown; IC_{50} fits ± s.e.m. are shown in the legend); norm., normalized. **c**, TEVC recordings of inward currents elicited by application of 100 μM uridine (Uri) or 100 μM NHC to hCNT3-expressing oocytes. Left, representative trace. Right, summary of peak currents from $n = 3$ biological replicates, with individual measurements and mean ± s.e.m. shown. Values are baseline corrected to leak current per oocyte. **d**, TEVC recordings of inward currents elicited by the application of 100 μM uridine or 400 μM GS4 in WT bCNT3-expressing oocytes. Left, representative trace. Right, summary of peak currents from $n = 4$ biological replicates. Values are baseline corrected to leak current per oocyte.

opposite to the nucleobase. Although this bulky group points away from TM7, it appears to affect the ribose interactions with bCNT3, as its ribose is shifted compared to NHC (Supplementary Fig. 3d,e), likely explaining its low CNT3 affinity and low-level evoked sodium currents in bCNT3 (Fig. 1b,d).

Ion binding sites

We assigned sodium ions and their coordination in the 2.31-Å-resolution GS4 consensus maps (Extended Data Fig. 4). The first sodium site, located ~7 Å from the nucleoside binding site with octahedral coordination (Extended Data Fig. 4), matches the single sodium site in bacterial CNTs[20] and is termed 'Na^+ site 1'. The 2:1 sodium:nucleoside ratio in hCNT3 (ref. 33) and previous studies[21,37] suggest an additional sodium site in bCNT3 proximal to C602 (C608 in bCNT3). We observed an oblong cryo-EM density peak consistent with sodium and water. The CMM server[38] aided in the assignment of sodium and water, exhibiting a square planar coordination (Extended Data Fig. 4). Intriguingly, this 'Na^+ site 2' is connected to Na^+ site 1 via the unwound portion of TM4 (Extended Data Fig. 4). We previously showed that sodium at Na^+ site 1 does not directly interact with the nucleoside, but its occupancy stabilizes the nucleoside binding pocket, thereby enhancing its nucleoside affinity[18,20]. The arrangement and proximity of Na^+ site 2 to the nucleoside binding pocket resemble those of Na^+ site 1, suggesting that the role of Na^+ site 2 is similar to that of Na^+ site 1 in modulating nucleoside affinity. Consistent with this, the CNT3 C602R variant, which has an altered stoichiometry of 1:1 for sodium/nucleoside, exhibits altered specificity for nucleoside drugs[39].

MPV-arrested OFS, INT1, INT2 and INT3 conformations

Previous bacterial CNT studies revealed elevator-type movements in apo states, representing the return path after nucleoside and sodium release[18]. However, elevator-type movements of a CNT with drug and sodium bound have yet to be elucidated.

Using TEVC, we found that MPV rapidly and reversibly reduces uridine-evoked inward currents in hCNT3 and bCNT3, indicating either that MPV transports through CNT3 very slowly or acts as an inhibitor (Extended Data Fig. 5a,b). We limited this competition TEVC experiment to MPV; ribavirin, GS4 and NHC are efficiently transported by CNT3 (Fig. 1a–d). This unanticipated result led us to posit that MPV might stabilize purified bCNT3 in conformational states different from the IFS. We used two approaches to introduce the drug into bCNT3 for cryo-EM grid preparation: (1) throughout protein purification ('condition 1') or just before freezing ('condition 2'; see Methods). In the condition 1 dataset, using both symmetry expansion with three-dimensional (3D) classification and 3D variability analysis, we identified three distinct non-IFS conformers in the protomer: (1) an outward-facing state (OFS), (2) an intermediate conformer in which the nucleoside binding site is completely occluded (termed 'INT1') and (3) a state close to the IFS ('INT3'; Extended Data Fig. 6a,b and Supplementary Table 3). In the condition 2 dataset, using symmetry expansion with 3D classification, we found two different non-IFS conformations within the protomer: (1) one nearly identical to INT1 in condition 1 and (2) a state distinct from both INT1 and INT3 (termed 'INT2'; Extended Data Fig. 7a,b and Supplementary Table 3). All four conformations (OFS, INT1, INT2 and INT3) feature robust cryo-EM densities for MPV (Extended Data Fig. 8).

https://doi.org/10.1038/s41589-024-01559-8

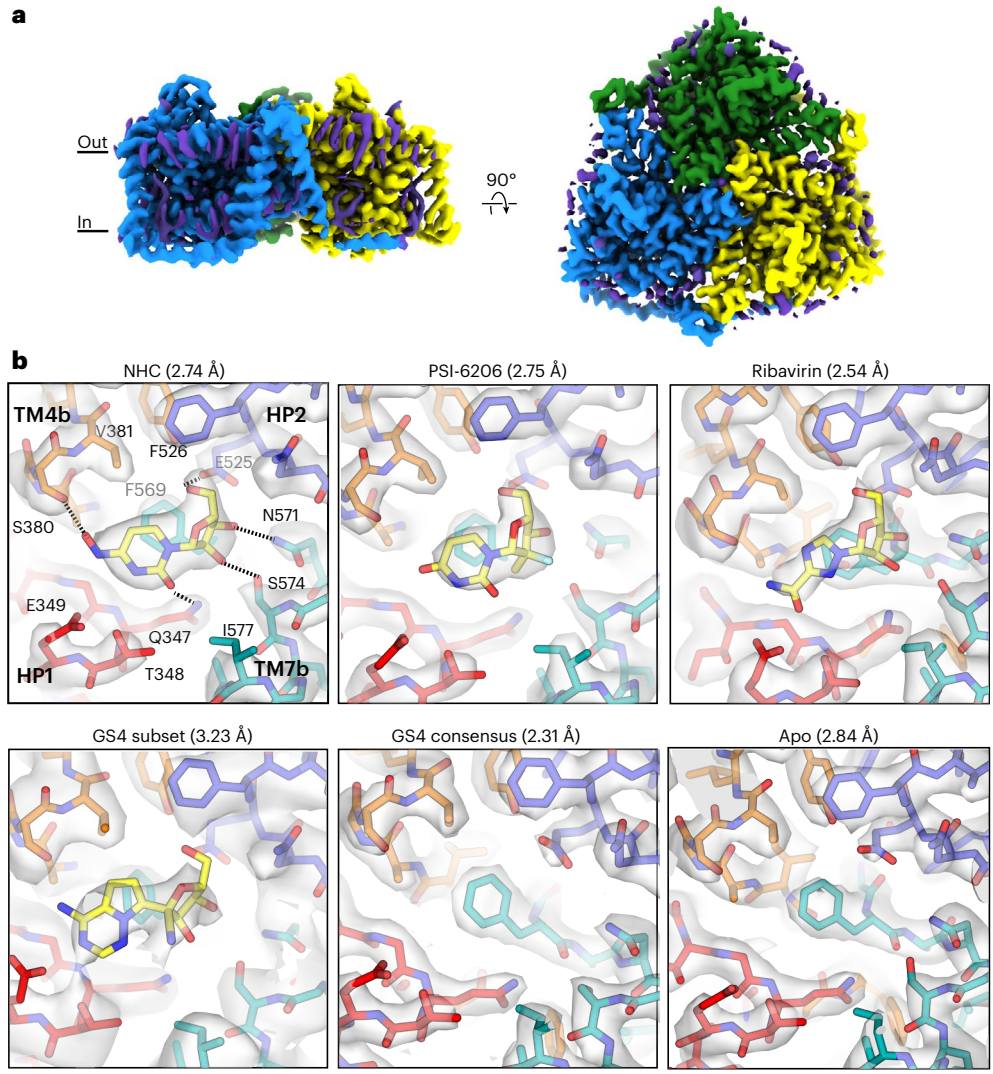

Fig. 2 | Cryo-EM structures of IFS bCNT3 in lipid nanodiscs. a, Representative cryo-EM reconstruction of trimeric bCNT3 in the IFS conformation (2.31 Å 'GS4 consensus', unsharpened map). Protein cryo-EM densities are colored by protomer, and non-protein lipid cryo-EM densities are depicted in purple. **b**, Transporter–drug interactions in additional drug-bound and drug-free states. For better comparison, cryo-EM maps shown here are low passed to 2.84 Å (NHC, PSI-6206, ribavirin and GS4 consensus and apo) or without low-pass filter (GS4 subset), followed by uniform map sharpening with −50 e^{-} $Å^{-2}$ post hoc B-factor applied. The true resolutions for these cryo-EM reconstructions are shown in parentheses. Cryo-EM densities are shown at map threshold values of 6σ for NHC, PSI-6206, ribavirin, GS4 subset and apo or 7σ for GS4 consensus.

Using TM3 and TM6 as alignment references, rigid body motions of the transport domain are apparent from the OFS to INT3 (Fig. 3a–c). The OFS-to-INT1 transition shows a large downward movement of the transport domain, whereas from INT1 to INT2 and INT3, the transport domain rotates with a small downward shift (Fig. 3b). INT1 features a cavity in which the solvent has no access to bound MPV from either side of the membrane, whereas the rotations from INT1 to INT2 and INT3 progressively expose this cavity to the intracellular solution (Fig. 3a). Hence, the elevator-type transport domain motions slide the nucleoside binding site across TM3 and TM6 by ~11 Å, accompanied by a ~15° rotation (Fig. 3b,c).

State-dependent solvent accessibility changes to the nucleoside pocket result from varied interactions between the transport and scaffold domains. In the OFS, TM7b and HP1 pack against TM3 and TM6, forming an intracellular gate (Fig. 3d). In the IFS, TM4b and HP2 pack against TM3 and TM6, forming an extracellular gate. These motions alternately form or break two gates, underlying the alternating access mechanism of the NAA-loaded carriers (Fig. 3d). The transport domain in INT1 features simultaneous engagement of both extracellular and intracellular gates, representing a drug- and sodium-bound fully occluded state (Fig. 3a,d). The previous bacterial CNT study showed apo-intermediate states midway between the OFS and IFS[18]. In stark contrast, the drug-loaded intermediate states here are closer to the IFS (Extended Data Fig. 9a,b).

Contribution of the switch of HP2 to transport dynamics

Our data indicate that MPV is either a low-turnover substrate or an inhibitor of CNT3 (Fig. 1b and Extended Data Fig. 5a,b). How does MPV stabilize various bCNT3 conformations? Alignment of the transport domains of non-IFSs to an IFS structure (NHC bound) reveals that the key structural difference is the side chain rotamer change of F526 on HP2. The 5′-isopropyl ester PG of MPV contacts F526, causing its reorientation without affecting other side chains in the binding pocket (Extended Data Fig. 9c). Notably, this change in the F526 rotamer conformation impacts its local interaction network with the scaffold domain (Fig. 3e). In the OFS conformation, this 5′-PG of MPV is sandwiched between F526 and phenylalanine residues on the scaffold domain (F289 and F290; Fig. 3e), making the transport domain transition from the OFS to INT1

https://doi.org/10.1038/s41589-024-01559-8

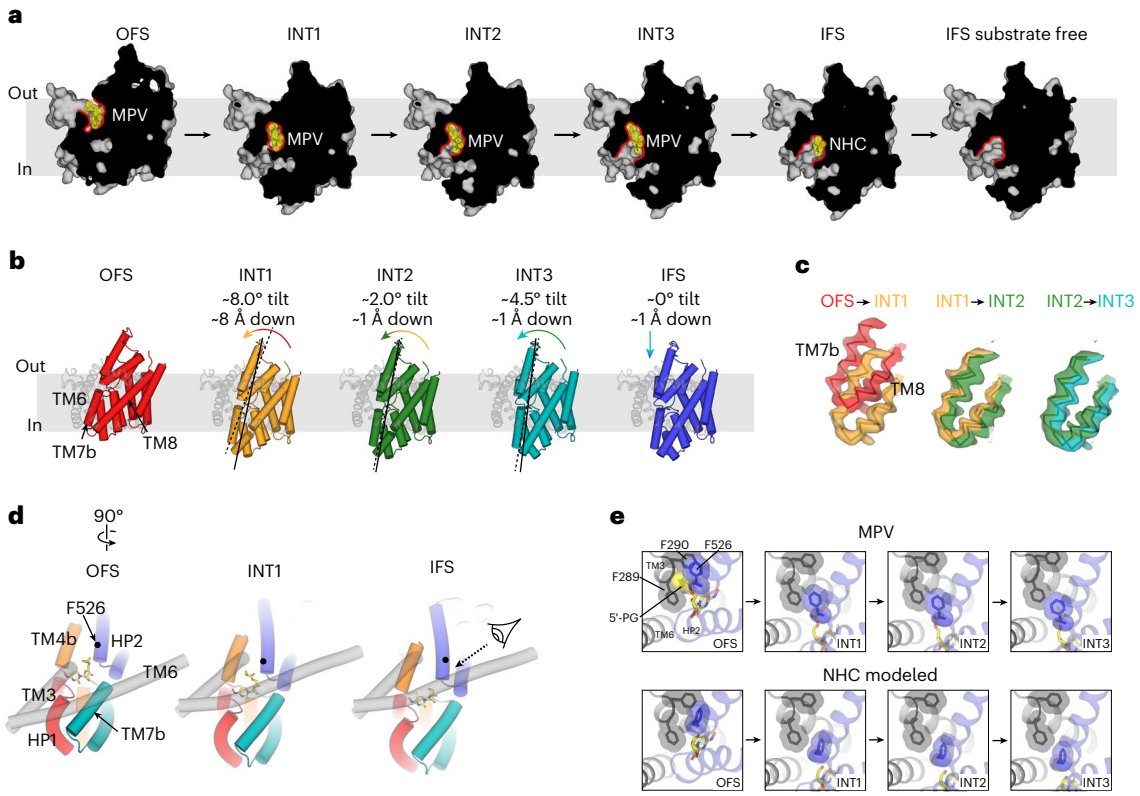

Fig. 3 | Alternating access of MPV-loaded bCNT3. a, Surface representation of OFS, INT1, INT2, INT3 or IFS. MPV and NHC are shown as sticks with yellow highlighting. The cavity outline is highlighted with a red line. **b**, Rigid body transitions of the transport domain (tube cartoon, colored) relative to the scaffold domain (cartoon, gray) in all five elucidated conformational states. Lines serve as an approximate reference for the transport domain tilt angle, with dotted lines representing the previous conformer in the trajectory and solid lines representing the current conformer. **c**, Cryo-EM map to model for the TM7b–TM8 turn in stepwise transitions from the OFS to INT1, INT1 to INT2 and INT2 to INT3 (maps were low-pass filtered to 4.5 Å for comparison). **d**, Components of the extracellular gate (HP2 and TM4b) and the intracellular gate (HP1 and TM7b) in the OFS, INT1 and IFS, with relative positions of the scaffold domain elements TM3 and TM6 shown for reference. **e**, Top, interactions between F526 and HP2 with the 5′-PG of MPV and F289 and F290 of the scaffold domain in the OFS, INT1, INT2, INT3 and IFS. Bottom, the transport domain of the NHC structure modeled onto the conformers by structural superposition.

(or IFS) difficult. However, the F526 alternate rotamer, when modeled, seems to slide more easily past F289 of the scaffold domain (Fig. 3e). The modeled alternate F526 rotamer would be poised to form optimal π–π interactions with F289 as it slides past it in the three intermediate states (Fig. 3e). These findings provide insights into the transport mechanism of CNT3. When in its optimal side chain conformation, F526 would mediate favorable interactions with the scaffold domain in the transient intermediate states, facilitating smoother transitions. When NAA bearing a bulky 5′-PG is loaded, F526 adopts a different rotamer, acting as a 'steric switch' and hindering efficient sliding of the transport domain (Fig. 3e). We found that non-aromatic side chain substitutions of F526 decreased uptake activity for [^{3}H]ribavirin, suggesting the need for an aromatic side chain at position 526 for nucleoside transport (Extended Data Fig. 9d).

To test the F526 steric switch hypothesis, we conducted all-atom molecular dynamics (MD) simulations (Fig. 4). We postulated that (1) when MPV binds to CNT3 in the OFS, a combination of the activated F526 steric switch and the bulky 5′-PG of MPV would hinder the OFS-to-INT transition, and (2) in INT1, the activated F526 steric switch stabilizes INT1, making the INT1-to-INT2 transition more difficult.

We chose the INT1–INT1–OFS trimer structure with MPV for our MD simulation studies. For comparison, we also generated a model in which MPV was replaced with NHC (without a 5′ substituent) and the 'steric switch' was turned off (Fig. 4a). We performed two types of all-atom MD simulations: (1) standard MD without restraints and (2) steered MD (SMD) for the OFS-to-INT1 transition (see Methods and Supplementary Tables 4 and 5).

We first monitored NAA-bound bCNT3 dynamics through ligand r.m.s.d. relative to the binding pocket in standard MD simulations. There are five replicas, with each replica containing a trimer with two INT1 and one OFS conformers, ten INT1 and five OFSs in total. After 500 ns, out of ten INT1 conformers, six with NHC and eight with MPV remained bound (Fig. 4b). Notably, NHCs in INT1 (Fig. 4b) exhibited larger deviations than MPVs (Fig. 4b). Interestingly, four of ten INT1 conformers with NHC transitioned into an IFS-like conformation, releasing NHC into the cytoplasm (Supplementary Fig. 6). This is consistent with the idea that INT1 is a metastable state with greater stability when MPV is bound and is closer to the IFS than the OFS in its energetic landscape. We also observed that more MPVs (three of five) stay bound in the OFS conformer than NHCs (one of five; Fig. 4c). The OFS-to-INT1 transition was not observed during the standard MD simulations.

Using SMD simulations, we monitored the conformational transitions of ligands and the transport domain (binding pocket) with r.m.s.d. per SMD frame relative to the starting OFS and INT1 conformations. When NHC was bound and the steric switch was off (Fig. 4d), r.m.s.d. values of both NHC and the binding pocket relative to the OFS reference increased linearly and those relative to the INT1 decreased linearly with a minimum at ~14 ns. This illustrates that the transport domain transitions from the OFS to INT1 with NHC bound during SMD runs (Fig. 4d,e). By contrast, in SMD runs in which the MPV OFS structure was used as the starting frame, the MPV r.m.s.d. and binding pocket r.m.s.d. relative to the references (OFS or INT1) did not change coherently but fluctuated, suggesting an unsuccessful

https://doi.org/10.1038/s41589-024-01559-8

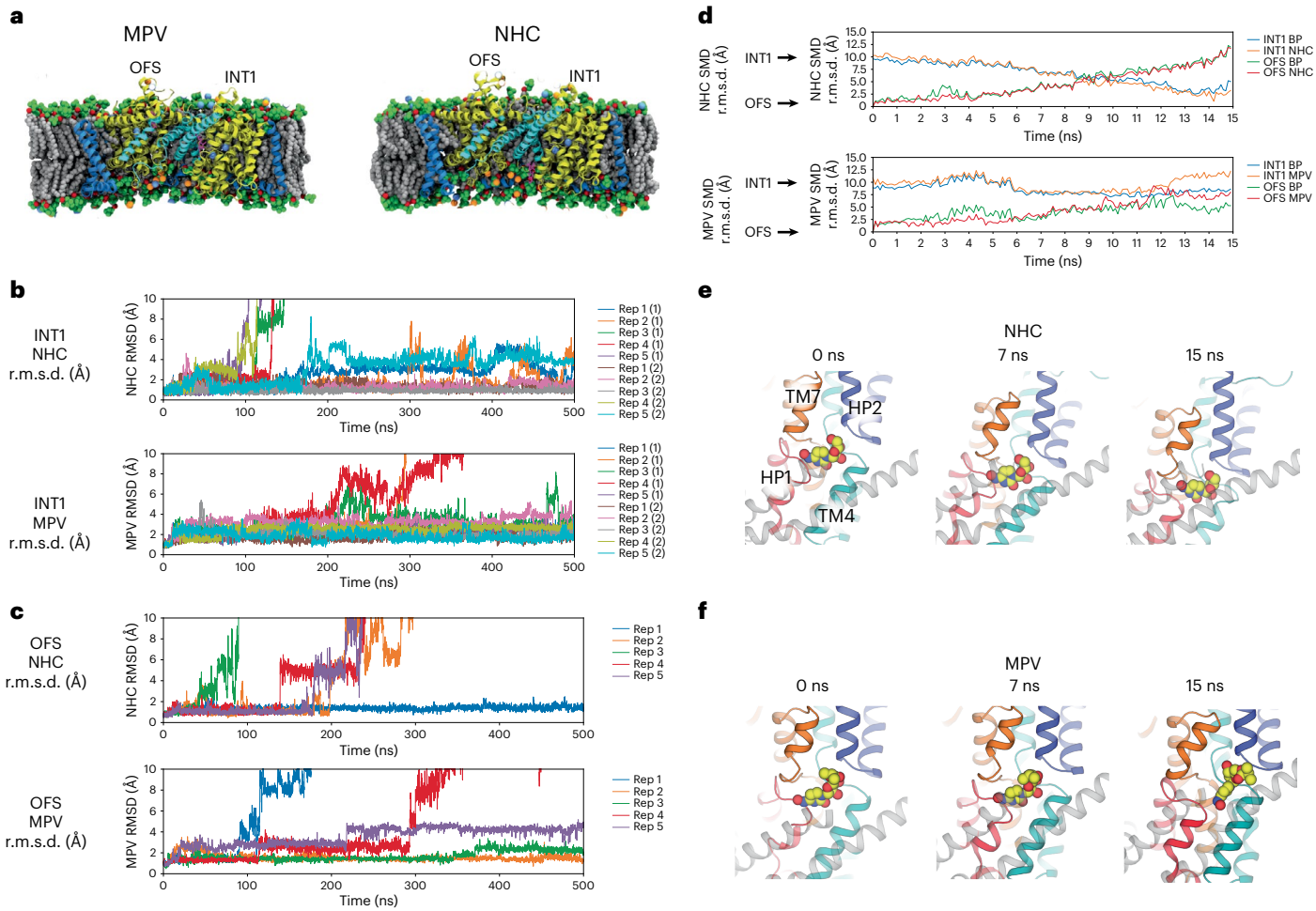

Fig. 4 | All-atom MD simulations of CNT3 transport dynamics. a, Simulation systems for the bCNT3 trimer with either MPV (left) or NHC (right) in the INT1–INT1–OFS trimer structure embedded in a mixed lipid bilayer in 150 mM NaCl. **b**, Standard all-atom MD simulation of the INT1 with NHC (top) or MPV bound (bottom). **c**, Standard all-atom MD simulation of OFS with NHC (top) or MPV bound (bottom). **d**, SMD simulations of NHC from the OFS to INT1 (top) and MPV from the OFS to INT1 (bottom); r.m.s.d. time series were calculated based on drug relative to the binding pocket (BP) in the OFS or INT1. **e**, Representative frames from SMD simulations of NHC-bound bCNT3 from the OFS to INT1. **f**, Representative frames from SMD simulations of MPV-bound bCNT3 from the OFS to INT1.

conformational transition (Fig. 4d,f). This result is consistent with our hypothesis that the steric switch, influenced by either prodrug or free NAA, alters the interface between the transport and scaffold domains, impacting the energetic landscape of the elevator-like movement (Supplementary Fig. 7).

Implications for rational drug modification

Our discovery concerning the role of F526 on HP2 as a steric switch suggests recommendations for drug modifications of existing NAAs. Decreasing the 5′-PG size in MPV may enhance its transportability through hCNT3 in intestinal epithelial apical membranes, potentially increasing its intestinal uptake and improving oral drug bioavailability. Previous in vitro studies on hCNT3 imply this strategy's feasibility, as NAAs bearing modest 5′ modifications can still translocate efficiently[40]. Ribose hydroxyl modifications are an attractive strategy for enhancing NAA pharmacological properties; for example, recent efforts have been focused on ribose hydroxyl-substituted GS4 analogs that have shown promise in preclinical studies[10,41,42]. In fact, a GS4 prodrug featuring the same 5′ isopropyl ester PG as MPV (obeldesivir) is currently in phase III clinical trials for the treatment of coronavirus disease 2019 (ref. 43). Therefore, the structural finding presented here has broad-reaching implications for drug modification of any NAA with a 5′-PG.

Comprehensive cryo-electron microscopy ensembles of transporter trimers

Our cryo-EM studies of bCNT3 reveal large elevator-like motions within the transport domain of the protomer. Do neighboring subunits 'feel' these motions as cooperativity? Previous studies on excitatory amino acid transporters, another type of trimeric elevator mechanism transporter, implicated subunit independence[44–46], but it remains unclear for CNTs.

Conventional classification strategies to isolate oligomeric arrangements in trimeric elevator-type transporters led to incomplete cryo-EM ensembles that converged well in the form of high-resolution 3D reconstructions[44,47]. We devised an image processing scheme to identify intersecting particle pick locations for every possible combination of protomer conformers (classes from symmetry expansion) and obtained cryo-EM reconstructions for every possible trimeric arrangement from the MPV condition 1 and condition 2 datasets (Fig. 5, Extended Data Figs. 6, 7, 9 and 10 and Methods). The 15 reconstructions reflect a total of 14 unique trimeric arrangements and range in resolution from 3.00 Å to 6.92 Å. The lowest-resolution trimer reconstructions are from rare states with low particle numbers (Fig. 5 and Extended Data Figs. 6, 7 and 10).

The population distributions of these trimeric arrangements conform to those calculated using raw frequencies of the protomer

https://doi.org/10.1038/s41589-024-01559-8

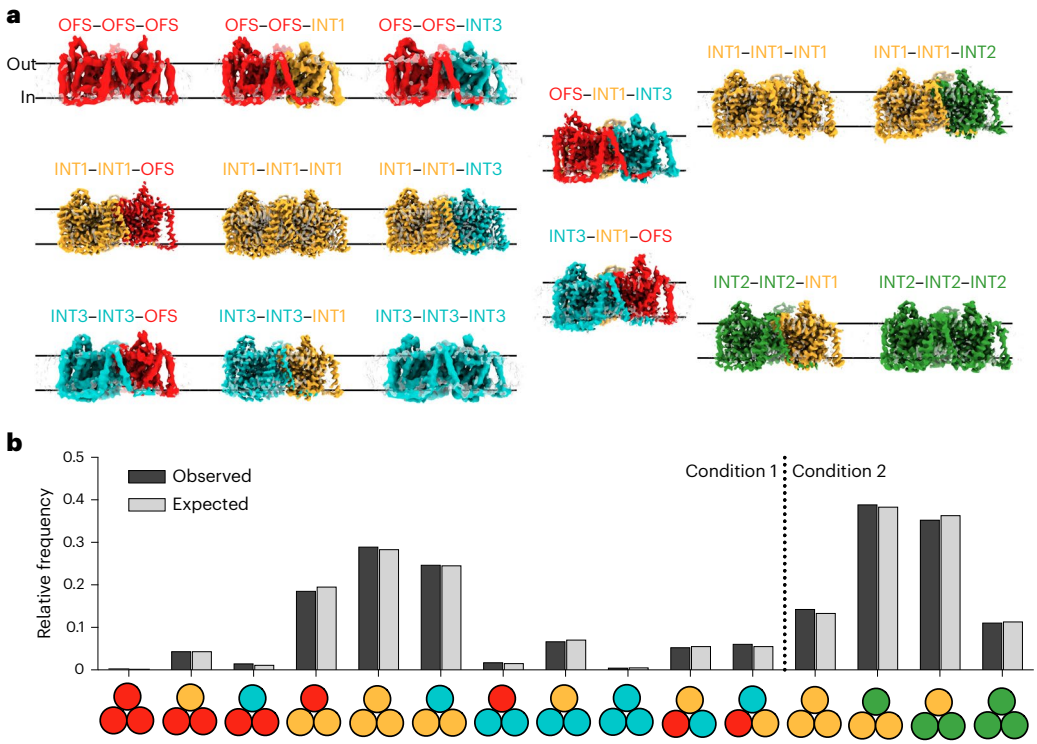

Fig. 5 | Cryo-EM ensembles of bCNT3 trimers. a, Cryo-EM reconstructions of each of the isolated trimeric states obtained from the ensemble analysis (the cryo-EM surface is colored by assigned conformer). **b**, Population distributions of trimer particles in the MPV condition 1 and condition 2 datasets. Observed relative frequencies represent relative particle distribution after classification and trimer identification. Expected relative frequencies (assuming a normal distribution) derived from raw symmetry expanded protomer populations before trimer identification (Methods).

classes with a normal distribution (Fig. 5). Any form of bias (positive or negative cooperativity) would have led the distribution of trimeric arrangements to deviate from a normal distribution. This is therefore the first line of experimental evidence that protomer movements within a CNT3 trimer are independent of each other. Future biophysical studies would be needed to corroborate this observation.

State-dependent changes in the local lipid environment

Our findings on the independence of subunits within the trimer raise a question about how this is achieved given that the transport domain undergoes such substantial movements. We inspected structurally superposed OFS–INT1–INT1, INT1–INT1–INT1 and INT3–INT1–INT1 bCNT3 trimers (the structural alignment was based on two of the INT1 protomers). We found that the scaffold domain is not static but exhibits considerable conformational changes that track with the transport domain movement (Fig. 6a,b). The eukaryotic scaffold domain appears to undergo the largest deformations, likely owing to the fact that $TM3^{Eu}$ directly leads into TM1 of the transport domain (Supplementary Fig. 2). From the OFS to INT1, $TM3^{Eu}$ exhibits a downward displacement of ~3 Å and a swinging motion of ~2 Å from INT1 to INT3 (Fig. 6b). This movement appears to be dissipated along the rest of the eukaryotic scaffold domain, as $TM1^{Eu}$–$TM2^{Eu}$ are relatively static, with $IH2^{Eu}$ serving as the hinge (Fig. 6a,b).

Notably, the well-ordered layers of lipids also track with the transport domain and eukaryotic scaffold domain movements (Fig. 6c,d). One well-defined lipid density, tentatively assigned as phosphatidylcholine, is located in the inner leaflet in a crevice between the transport domain and $TM3^{Eu}$ in the OFS–INT1–INT1, INT1–INT1–INT1 and INT3–INT1–INT1 reconstructions. This lipid undergoes substantial displacements from the OFS to INT1 and the INT1 to INT3 (Fig. 6c,d), which also correlate to transport domain movements. Therefore, the elevator-like motion of bCNT3 significantly deforms the local membrane environment. The membrane deformations are expected for elevator-type transport[47,48], and the cost of hydrophobic mismatch would disfavor simple sliding of the transport domain in and out of the membrane bilayer. The eukaryotic scaffold domain assists with this process by allowing efficient sliding of lipids located at crevices between the transport and scaffold domains. This buffers the surrounding bilayer environment from the local deformations induced by transport domain movements (Fig. 6e).

Discussion

Nucleoside transporters are important players in NAA drug pharmacology, as they control their target access and disposition[32]. Our bCNT3 cryo-EM structures shed light on drug selectivity within the binding pocket and the intricate arrangement of the two sodium binding sites, which aligns with the current 'affinity control' model for sodium-coupled nucleoside transport by CNTs, wherein sodium occupancy affects the binding pocket's structure and nucleoside affinity[18,32].

Interestingly, the architecture of the bCNT3 substrate and sodium binding sites bears a vague resemblance to what has been reported in SLC1, an unrelated family of elevator-type transporters (Supplementary Fig. 8). How two unrelated protein families evolved to use similar mechanistic strategies for vastly different substrates poses interesting questions regarding transporter evolution.

The unique interactions between MPV and bCNT3 enabled us to capture cryo-EM structures in outward-facing and intermediate states, providing insights into its transport mechanism. Notably, INT1 exhibits a fully occluded state, which is generally thought to be only transiently occupied during transporter isomerization[49,50]. We found that the F526 steric switch plays an important role in arresting this rare conformational state by MPV. During the transport of NHC, or transport of any NAA without a bulky 5′ substituent, F526 forms optimal

https://doi.org/10.1038/s41589-024-01559-8

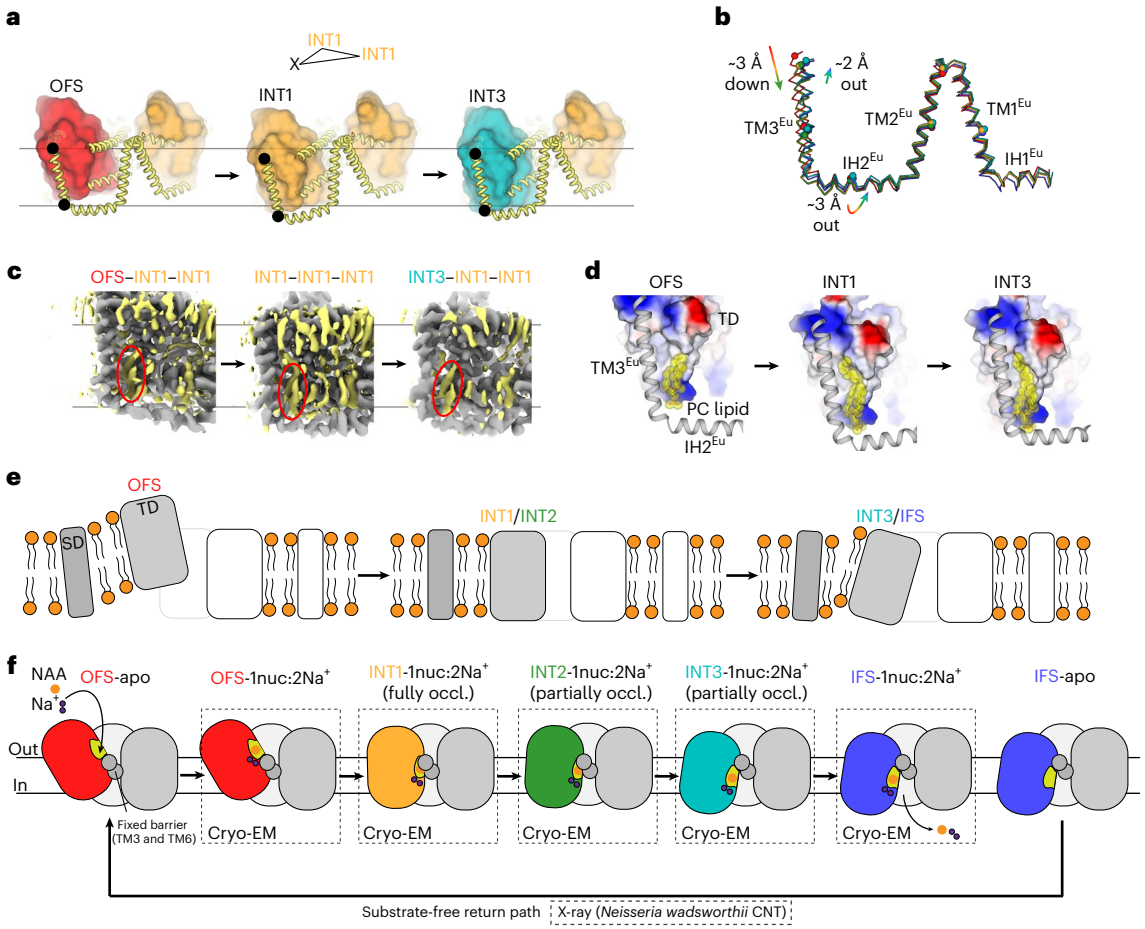

Fig. 6 | Scaffold domain and local lipid bilayer deformations during transport domain movements. a, Structural overlay of OFS–INT1–INT1, INT1–INT1–INT1 and INT3–INT1–INT1 trimers, highlighting the changes in the scaffold domain during conformational transitions (the transport domain is shown as colored surfaces, and the scaffold domain is shown as a thick yellow cartoon; the alignment is targeted on the two INT1 protomers). **b**, Overlay of the eukaryotic scaffold domain from all five conformers reported in this study (the alignment is targeted to the trimerization interface of TM3 and TM6; the ribbon depiction follows the same color scheme as in Figs. 3 and 4; spheres are shown to indicate the Cα of select marker residues). **c**, Overlayed OFS–INT1–INT1, INT1–INT1–INT1 and INT3–INT1–INT1 cryo-EM reconstructions (the map alignment is targeted to the two INT1 protomers), with non-protein densities shown in yellow. A lipid-like density sandwiched between $TM3^{Eu}$ and the transport domain (TD) is circled in red in each conformational state. **d**, Displacement of the modeled phosphatidylcholine (PC) molecule in the OFS, INT1 and INT3 conformational states relative to the transport domain (shown as surface colored by surface electrostatics) and eukaryotic scaffold domain (shown as a gray cartoon). **e**, Schematic for the role of the scaffold domain (SD) in assisting local membrane deformation during translocation of antiviral drugs. **f**, Current working model for the alternating access mechanism of antiviral drug transport by CNT3; occl., occluded.

interactions with the scaffold domain in the occluded intermediate states. In the case of MPV, or any NAA featuring a bulky 5′-PG group, the drug 'flips on' this F526 switch, promoting a different rotamer conformation. This in turn rearranges the interface present between the transport and scaffold domains in the normally short-lived intermediate states. Our structural analysis and all-atom MD simulations suggest that the changes in the interface either stabilize each state (for example, INT1) or elevate the energetic barriers between the states (for example, OFS to INT1), resulting in different energetic landscapes of the elevator-like motion with prodrug bound versus free NAA bound (Supplementary Fig. 7).

Our findings suggest implications to drug design. Using a smaller 5′-PG could keep the steric switch 'turned off', thereby enhancing the prodrug transportability through hCNT3 expressed in intestinal tissue, presumably improving its oral bioavailability. Although previous in vitro studies of hCNT3 support the feasibility of this strategy[40], because our structural studies were conducted using bCNT3, further research on hCNT3 is needed to investigate this possibility.

Finally, we found independent subunit movements within the trimer (Fig. 5). Combined with observed local membrane deformation in various conformations, the scaffold domain of CNT3 appears to function beyond just a trimerization interface. We suggest that it acts as an 'allosteric cushion', dissipating the local membrane deformations arising from large transport domain movements. This appears to limit the footprint of membrane deformation and prevent the propagation of conformational changes from affecting neighboring subunits within the trimer (Fig. 6e,f).

Online content

Any methods, additional references, Nature Portfolio reporting summaries, source data, extended data, supplementary information, acknowledgements, peer review information; details of author contributions and competing interests; and statements of data and code availability are available at https://doi.org/10.1038/s41589-024-01559-8.

References

1. Yates, M. K. & Seley-Radtke, K. L. The evolution of antiviral nucleoside analogues: a review for chemists and non-chemists. Part II: complex modifications to the nucleoside scaffold. *Antivir. Res.* **162**, 5–21 (2019).

2. Seley-Radtke, K. L. & Yates, M. K. The evolution of nucleoside analogue antivirals: a review for chemists and non-chemists. Part 1: early structural modifications to the nucleoside scaffold. *Antivir. Res.* **154**, 66–86 (2018).
3. Pruijssers, A. J. & Denison, M. R. Nucleoside analogues for the treatment of coronavirus infections. *Curr. Opin. Virol.* **35**, 57–62 (2019).
4. Graci, J. D. & Cameron, C. E. Mechanisms of action of ribavirin against distinct viruses. *Rev. Med. Virol.* **16**, 37–48 (2006).
5. Beigel, J. H. et al. Remdesivir for the treatment of Covid-19—final report. *N. Engl. J. Med.* **383**, 1813–1826 (2020).
6. Lawitz, E. et al. Sofosbuvir for previously untreated chronic hepatitis C infection. *N. Engl. J. Med.* **368**, 1878–1887 (2013).
7. Jayk Bernal, A. et al. Molnupiravir for oral treatment of Covid-19 in nonhospitalized patients. *N. Engl. J. Med.* **386**, 509–520 (2022).
8. Mehellou, Y., Rattan, H. S. & Balzarini, J. The ProTide prodrug technology: from the concept to the clinic. *J. Med. Chem.* **61**, 2211–2226 (2018).
9. Warren, T. K. et al. Therapeutic efficacy of the small molecule GS-5734 against Ebola virus in rhesus monkeys. *Nature* **531**, 381–385 (2016).
10. Sheahan, T. P. et al. An orally bioavailable broad-spectrum antiviral inhibits SARS-CoV-2 in human airway epithelial cell cultures and multiple coronaviruses in mice. *Sci. Transl. Med.* **12**, eabb5883 (2020).
11. Yan, V. C. & Muller, F. L. Advantages of the parent nucleoside GS-441524 over remdesivir for Covid-19 treatment. *ACS Med. Chem. Lett.* **11**, 1361–1366 (2020).
12. Williamson, B. N. et al. Clinical benefit of remdesivir in rhesus macaques infected with SARS-CoV-2. *Nature* **585**, 273–276 (2020).
13. Feld, J. J. & Hoofnagle, J. H. Mechanism of action of interferon and ribavirin in treatment of hepatitis C. *Nature* **436**, 967–972 (2005).
14. Murphy, B. G. et al. The nucleoside analog GS-441524 strongly inhibits feline infectious peritonitis (FIP) virus in tissue culture and experimental cat infection studies. *Vet. Microbiol.* **219**, 226–233 (2018).
15. Agostini, M. L. et al. Small-molecule antiviral β-D-N^4-hydroxycytidine inhibits a proofreading-intact coronavirus with a high genetic barrier to resistance. *J. Virol.* **93**, e01348-19 (2019).
16. Toots, M. et al. Characterization of orally efficacious influenza drug with high resistance barrier in ferrets and human airway epithelia. *Sci. Transl. Med.* **11**, eaax5866 (2019).
17. Yoon, J. J. et al. Orally efficacious broad-spectrum ribonucleoside analog inhibitor of influenza and respiratory syncytial viruses. *Antimicrob. Agents Chemother.* **62**, e00766-18 (2018).
18. Hirschi, M., Johnson, Z. L. & Lee, S. Y. Visualizing multistep elevator-like transitions of a nucleoside transporter. *Nature* **545**, 66–70 (2017).
19. Johnson, Z. L. et al. Structural basis of nucleoside and nucleoside drug selectivity by concentrative nucleoside transporters. *eLife* **3**, e03604 (2014).
20. Johnson, Z. L., Cheong, C. G. & Lee, S. Y. Crystal structure of a concentrative nucleoside transporter from *Vibrio cholerae* at 2.4 Å. *Nature* **483**, 489–493 (2012).
21. Zhou, Y. et al. Cryo-EM structure of the human concentrative nucleoside transporter CNT3. *PLoS Biol.* **18**, e3000790 (2020).
22. Young, J. D., Yao, S. Y., Baldwin, J. M., Cass, C. E. & Baldwin, S. A. The human concentrative and equilibrative nucleoside transporter families, SLC28 and SLC29. *Mol. Asp. Med.* **34**, 529–547 (2013).
23. Wright, N. J. & Lee, S. Y. Structures of human ENT1 in complex with adenosine reuptake inhibitors. *Nat. Struct. Mol. Biol.* **26**, 599–606 (2019).
24. Wang, C. et al. Structural basis of the substrate recognition and inhibition mechanism of *Plasmodium falciparum* nucleoside transporter PfENT1. *Nat. Commun.* **14**, 1727 (2023).
25. Tsubota, A. et al. Contribution of ribavirin transporter gene polymorphism to treatment response in peginterferon plus ribavirin therapy for HCV genotype 1b patients. *Liver Int.* **32**, 826–836 (2012).
26. Doehring, A. et al. Role of nucleoside transporters SLC28A2/3 and SLC29A1/2 genetics in ribavirin therapy: protection against anemia in patients with chronic hepatitis C. *Pharmacogenet. Genomics* **21**, 289–296 (2011).
27. Rau, M. et al. Impact of genetic SLC28 transporter and ITPA variants on ribavirin serum level, hemoglobin drop and therapeutic response in patients with HCV infection. *J. Hepatol.* **58**, 669–675 (2013).
28. Iikura, M. et al. ENT1, a ribavirin transporter, plays a pivotal role in antiviral efficacy of ribavirin in a hepatitis C virus replication cell system. *Antimicrob. Agents Chemother.* **56**, 1407–1413 (2012).
29. Morello, J. et al. Influence of a single nucleotide polymorphism at the main ribavirin transporter gene on the rapid virological response to pegylated interferon–ribavirin therapy in patients with chronic hepatitis C virus infection. *J. Infect. Dis.* **202**, 1185–1191 (2010).
30. Rasmussen, H. B. et al. Cellular uptake and intracellular phosphorylation of GS-441524: implications for its effectiveness against COVID-19. *Viruses* **13**, 1369 (2021).
31. Wang, A. Q. et al. Preclinical pharmacokinetics and in vitro properties of GS-441524, a potential oral drug candidate for COVID-19 treatment. *Front. Pharmacol.* **13**, 918083 (2022).
32. Wright, N. J. & Lee, S. Y. Toward a molecular basis of cellular nucleoside transport in humans. *Chem. Rev.* **121**, 5336–5358 (2021).
33. Smith, K. M. et al. Cation coupling properties of human concentrative nucleoside transporters hCNT1, hCNT2 and hCNT3. *Mol. Membr. Biol.* **24**, 53–64 (2007).
34. Hamilton, S. R. et al. Subcellular distribution and membrane topology of the mammalian concentrative Na^+–nucleoside cotransporter rCNT1. *J. Biol. Chem.* **276**, 27981–27988 (2001).
35. Fernandez-Calotti, P., Casulleras, O., Antolin, M., Guarner, F. & Pastor-Anglada, M. Galectin-4 interacts with the drug transporter human concentrative nucleoside transporter 3 to regulate its function. *FASEB J.* **30**, 544–554 (2016).
36. Damaraju, V. L. et al. Influence of sugar ring conformation on the transportability of nucleosides by human nucleoside transporters. *ChemBioChem* **12**, 2774–2778 (2011).
37. Arimany-Nardi, C. et al. Identification and characterization of a secondary sodium-binding site and the main selectivity determinants in the human concentrative nucleoside transporter 3. *Mol. Pharm.* **14**, 1980–1987 (2017).
38. Gucwa, M. et al. CMM—an enhanced platform for interactive validation of metal binding sites. *Protein Sci.* **32**, e4525 (2023).
39. Errasti-Murugarren, E., Molina-Arcas, M., Casado, F. J. & Pastor-Anglada, M. The human concentrative nucleoside transporter-3 C602R variant shows impaired sorting to lipid rafts and altered specificity for nucleoside-derived drugs. *Mol. Pharmacol.* **78**, 157–165 (2010).
40. Zhang, J. et al. Uridine binding and transportability determinants of human concentrative nucleoside transporters. *Mol. Pharmacol.* **68**, 830–839 (2005).
41. Cao, L. et al. The adenosine analog prodrug ATV006 is orally bioavailable and has preclinical efficacy against parental SARS-CoV-2 and variants. *Sci. Transl. Med.* **14**, eabm7621 (2022).
42. Schafer, A. et al. Therapeutic treatment with an oral prodrug of the remdesivir parental nucleoside is protective against SARS-CoV-2 pathogenesis in mice. *Sci. Transl. Med.* **14**, eabm3410 (2022).
43. NCT05603143: Study of obeldesivir in participants with COVID-19 who have a high risk of developing serious or severe illness (BIRCH). https://clinicaltrials.gov/show/NCT05603143 (2022).

44. Qiu, B., Matthies, D., Fortea, E., Yu, Z. & Boudker, O. Cryo-EM structures of excitatory amino acid transporter 3 visualize coupled substrate, sodium, and proton binding and transport. *Sci. Adv.* **7**, eabf5814 (2021).
45. Erkens, G. B., Hänelt, I., Goudsmits, J. M., Slotboom, D. J. & van Oijen, A. M. Unsynchronised subunit motion in single trimeric sodium-coupled aspartate transporters. *Nature* **502**, 119–123 (2013).
46. Georgieva, E. R., Borbat, P. P., Ginter, C., Freed, J. H. & Boudker, O. Conformational ensemble of the sodium-coupled aspartate transporter. *Nat. Struct. Mol. Biol.* **20**, 215–221 (2013).
47. Arkhipova, V., Guskov, A. & Slotboom, D. J. Structural ensemble of a glutamate transporter homologue in lipid nanodisc environment. *Nat. Commun.* **11**, 998 (2020).
48. Garaeva, A. A. & Slotboom, D. J. Elevator-type mechanisms of membrane transport. *Biochem. Soc. Trans.* **48**, 1227–1241 (2020).
49. Drew, D., North, R. A., Nagarathinam, K. & Tanabe, M. Structures and general transport mechanisms by the major facilitator superfamily (MFS). *Chem. Rev.* **121**, 5289–5335 (2021).
50. Qureshi, A. A. et al. The molecular basis for sugar import in malaria parasites. *Nature* **578**, 321–325 (2020).

Methods

Radiotracer uptake in transporter-expressing *X. laevis* oocytes

[^{3}H]Ribavirin was purchased from Moravek. Defolliculated *X. laevis* oocytes were obtained from Xenopus 1. Uptake assays were performed in a manner similar to a previous report[51], with the following modifications. A total of 16–20 ng of cRNA (coding RNA) was injected per oocyte, with expression performed at 17 °C for 2–4 d. A reaction volume of 200 µl was used, and [^{3}H]ribavirin was used at full radioactivity in every experiment (6.5 Ci mmol^{-1}). Oocytes were batched by five per reaction vessel. For all ENT isoforms, oocytes were washed extensively in normal ND-96 buffer (96 mM NaCl, 2 mM KCl, 1 mM $MgCl_2$, 1.8 mM $CaCl_2$ and 5 mM HEPES, pH 7.4 with KOH) to terminate the uptake reaction, whereas sodium-free ND-96 buffer (NaCl replaced with choline chloride) was used for assay termination and washing for all CNT isoforms assessed.

Two-electrode voltage-clamp recording of transporter-expressing *X. laevis* oocytes

Oocytes expressing transporters of interest were studied using the TEVC technique. For the recording, oocyte membrane voltage was controlled using an OC-725C oocyte clamp (Warner Instruments). Data were filtered at 1–3 kHz and digitized at 20 kHz using pClamp 10.6 software (Molecular Devices) and a Digidata 1550 digitizer (Axon Instruments). Microelectrode resistances were 0.5–2 MΩ when filled with 3 M KCl. ND-96 buffer was used as external recording solution. All nucleosides and nucleoside analog drugs were applied using a gravity-fed perfusion system. Recordings were performed in episodic stimulation recording mode. The voltage was initially held at 0 mV for 50 ms, followed by a step to −60 mV (bCNT3) or −90 mV (hCNT3) for 300 ms and then a step back to 0 mV for 50 ms, with a sweep happening every 2 s. All electrophysiological data analyses were performed using Igor Pro 6.34A (Wavemetrics).

Expression, purification and nanodisc reconstitution of bCNT3

Full-length WT bCNT3 sequence (UniProt ID F1MGR1) was synthesized in the pFastBac vector containing a Flag tag (DYKDDDDK) at the N terminus of the protein. Baculovirus was generated in *Spodoptera frugiperda* Sf9 insect cells using standard protocols and amplified to passage 2 (P2). Insect cells were infected with 1% (vol/vol) high-titer P2 virus at a cell density of 1×10^6–1.5×10^6 cells per ml. Protein expression was performed at 27 °C for 72 h, after which cells were collected by centrifugation at 550*g*. Cell pellets were resuspended in ice-cold lysis buffer (50 mM Tris (pH 8.0), 150 mM NaCl, 1 mM phenylmethylsulphonyl fluoride, 10 µg ml^{-1} leupeptin, 10 µg ml^{-1} pepstatin, 1 µg ml^{-1} aprotinin and 2 mg ml^{-1} iodoacetamide) at ~1 g of cell pellet per 4 ml of crude lysate. Resuspended cells were then subjected to three rounds of sonication on ice (30 s, one pulse per s). A final concentration of 40 mM *n*-dodecyl-β-D-maltoside detergent was added to the disrupted cells, and detergent extraction was performed for 1 h at 4 °C with gentle agitation. Insoluble material was then removed by centrifugation at 30,000*g* for 30 min. Clarified lysate was then applied to anti-Flag M2 resin at 4 °C with gentle agitation for 1 h. During resin binding, a stock of PCEG synthetic lipid mixture (10 mg ml^{-1}) was prepared in the following manner. Chloroform stocks (10 mg ml^{-1}) of 16:0–18:1 PC (Avanti, 850457), 14:0 PE (Avanti, 850745P) and 14:0 PG (Avanti, 840445P) were combined in a 3:1:1 (vol/vol/vol) ratio, respectively. The chloroform mixture was vortexed and dried under gentle argon gas flow in a glass tube. The solid lipids were resuspended in 0.5 initial volume pentane, vortexed briefly and dried again under argon gas flow. The solid lipid was then resuspended in 1.0 initial volume 20 mM Tris (pH 8.0) and 150 mM NaCl buffer and passed through an extruder loaded with a 0.2-µm Whatman filter ~30 times. At the conclusion of Flag resin binding, resin was then collected by gentle centrifugation (550*g*) and resuspended in one column volume of wash buffer (20 mM Tris (pH 8.0), 150 mM NaCl, 1.0 mM *n*-dodecyl-β-D-maltoside and 0.1 mg ml^{-1} added PCEG lipids). The resuspended resin slurry was added to a gravity flow column and washed with ten column volumes of wash buffer. Protein was eluted from the column in wash buffer supplemented with 0.2 mg ml^{-1} Flag peptide. Protein concentration was estimated at an optical density at 280 nm and combined with MSP2N2 protein and PCEG lipids at a final molar ratio of 1:3:200 bCNT3 trimer:MSP2N2 protein:PCEG lipids. The mixture was incubated on ice for 1 h and transferred to a fresh tube containing degassed Bio-Bead SM-2 resin (Bio-Rad) at a final concentration of ~100 mg ml^{-1} beads. After 2 h of incubation with gentle agitation, the beads were replaced, and incubation was performed overnight at 4 °C with gentle agitation. The reconstitution mixture was then removed from the beads and spun down at 20,000*g* for 30 min before injection over a size-exclusion chromatography (SEC) column (Superose 6 Increase 10/300 GS, Cytiva) pre-equilibrated in 20 mM Tris (pH 8.0) and 150 mM NaCl. Protein was usually prepared in the absence of drug, with the following exceptions. For the NHC structure, drug was present at 100 µM during lysis, resin binding and resin washing, 1.0 mM was present in the resin elution buffer, 1.0 mM was present at all times during Bio-Bead treatment, and SEC was performed in the absence of drug. For the GS4 structure, drug was present at 300 µM during lysis, resin binding and resin washing, 1.0 mM was present in the resin elution buffer, 1.0 mM was present at all times during Bio-Bead treatment, and SEC was performed in the absence of drug. An additional 2 mM drug was added to pooled fractions before concentration for grid freezing. For MPV condition 1 protein, drug was present at 1.0 mM during lysis, 0.5 mM during resin binding, resin washing and resin elution, three 0.5 mM additions were added during Bio-Bead treatment, and SEC was performed in the absence of drug.

Cryo-electron microscopy sample preparation

Peak fractions from SEC were pooled and concentrated to a final concentration of 7–10 mg ml^{-1} before grid preparation. Drug stocks were added after sample concentration and allowed to incubate on ice for ~1 h to grid freezing with the following final concentrations: 2 mM NHC (2% DMSO final), 19.2 mM PSI-6206 (2% DMSO final), 25 mM GS4 (5% DMSO final), 2 mM ribavirin (2% DMSO final), 7.5 mM MPV (MPV condition 1, 2% DMSO final), 15 mM MPV (MPV condition 2, 2% DMSO final) and drug-free (2% DMSO final). Grids were prepared with a Leica EM GP2 Plunge Freezer operating at 4 °C at 95% humidity. To address preferred orientation issues of nanodisc reconstituted bCNT3, fluorinated fos-choline-8 (Anatrace) was rapidly added to 3 µl of protein to a final concentration of 3 mM and rapidly aspirated 5 times (from 30 mM stock of fluorinated fos-choline-8 in 20 mM Tris (pH 8) and 150 mM NaCl). In under 10 s from fluorinated fos-choline-8 addition, samples were quickly applied to a freshly glow-discharged Quantifoil Au R1.2/1.3 300 mesh grid, blotted with Whatman No. 1 filter paper for 3 s and plunge-frozen in liquid ethane.

Cryo-electron microscopy data collection

The drug-free, PSI-6206, ribavirin, MPV condition 1 and MPV condition 2 datasets were collected on a Titan Krios (Thermo Fisher) transmission electron microscope operating at 300 kV equipped with a K3 camera (Gatan) in counting mode and BioQuantum GIF energy filter with a slit width of 20 eV, using Latitude S (Gatan) for image acquisition (Duke University Shared Materials Instrumentation Facility (SMIF)). The magnification for these datasets was ×81,000, with a physical pixel size of 1.08 Å per pixel. In total, 40 frames were acquired for each movie with a 2.4-s exposure time and a nominal dose rate of ~30 e^- per pixel per s for a total dose of ~60 e^- Å^{-2} and a defocus range of −0.8 to −1.8 µm.

The NHC and GS4 datasets were collected on a Titan Krios (Thermo Fisher) transmission electron microscope operating at 300 kV equipped with a K3 camera (Gatan) in counting mode and BioQuantum GIF energy filter with a slit width of 20 eV, using Latitude S (Gatan)

for image acquisition (National Cancer Institution National Cryo-EM Microscopy Facility (NCEF)). The magnification for these datasets was ×81,000, with a physical pixel size of 1.12 Å per pixel for the NHC dataset or 1.08 Å per pixel for the GS4 dataset. In total, 40 frames were acquired for each movie, with a 4.4-s or 3.3-s exposure time for NHC and GS4, respectively. The nominal dose rate was 17.1 e^- per pixel per s for the NHC dataset and 17.7 e^- per pixel per s for the GS4 dataset. The total dose was 60 e^- $Å^{-2}$ for the NHC dataset and 50 e^- $Å^{-2}$ for the GS4 dataset. A defocus range of −1.00 to −2.25 µm was used for the NHC dataset, and a defocus range of −1.0 to −2.0 µm was used for the GS4 dataset.

Cryo-electron microscopy data processing: standard procedures

Apo. In total, 2,622 movies were subjected to MotionCorr2 in Relion[52] and CTFFIND4 in cryoSPARC[53]. Micrographs exhibiting a contrast transfer function (CTF) estimated resolution under 6 Å were selected and subjected to template picking in cryoSPARC. After manual curation of pick locations, particles were extracted with a box size of 64 pixels with 4× Fourier binning (4.32 Å per pixel). A total of 2.2 million extracted particles were subjected to two-dimensional (2D) classification. Two-dimensional classes featuring strong protein features were then re-extracted with a box size of 128 pixels and 2× binning (2.16 Å per pixel), followed by a $k = 4$ heterogenous refinement with C3 symmetry applied. The highest resolution class was then re-extracted with a box size of 256 pixels with no binning (1.08 Å per pixel) and subjected to non-uniform refinement with C3 symmetry applied. The particle stack and angular priors were then transferred to Relion for two rounds of Bayesian polishing. The shiny particles were reimported into cryoSPARC for a final round of non-uniform refinement with C3 symmetry applied, resulting in a 2.80-Å final reported resolution (Fourier shell correlation (FSC) = 0.143).

NHC. In total, 7,243 movies were subjected to MotionCorr2 in Relion[52] and Gctf in Relion for CTF estimation. Micrographs featuring a rlnFigureOfMerit of >0.07 were selected and subjected to template picking in Relion. Particles were then extracted with a box size of 64 pixels with 4× Fourier binning (4.48 Å per pixel). A total of 1.7 million extracted particles were subjected to 2D classification. Two-dimensional classes featuring strong protein features were then re-extracted with a box size of 128 pixels and 2× binning (2.24 Å per pixel), followed by autorefine and no-image alignment classification ($k = 2$/tau_fudge = 20), with C3 symmetry applied. The highest resolution class was then re-extracted with a box size of 256 pixels with no binning (1.12 Å per pixel) and subjected to another round of autorefine and no-alignment classification ($k = 2$/tau_fudge = 20). The highest resolution class, containing 175,676 particles, was subjected to CTF refinement and Bayesian polishing. The particle stack and angular priors were then transferred to cryoSPARC and subjected to a round of heterogenous refinement ($k = 3$), with 147,332 particles in the best class. This particle stack was subjected to a final round of non-uniform refinement followed by local refinement, both with C3 applied, to a final resolution of 2.74 Å (FSC = 0.143). After obtainment of numerous other bCNT3 IFS reconstructions, the cryo-EM map obtained for NHC appeared slightly dilated compared to all other reconstructions. A model-based pixel size calibration was performed in which the map-to-model correlation (determined in Phenix[54]) was highest with a pixel size set to 1.11 Å. All maps for this structure are deposited with the pixel size set to 1.11 Å.

PSI-6206. In total, 3,820 movies were subjected to MotionCorr2 in Relion[52] and CTFFIND4 in cryoSPARC[53]. Micrographs exhibiting a CTF estimated resolution under 6 Å were selected and subjected to template picking in cryoSPARC. After manual curation of pick locations, particles were extracted with a box size of 64 pixels with 4× Fourier binning (4.32 Å per pixel). A total of 2.8 million extracted particles were subjected to 2D classification. Two-dimensional classes featuring strong protein features were then re-extracted with a box size of 128 pixels and 2× binning (2.16 Å per pixel), followed by a $k = 3$ heterogenous refinement with C3 symmetry applied. The highest resolution class was then re-extracted with a box size of 256 pixels with no binning (1.08 Å per pixel) and subjected to non-uniform refinement with C3 symmetry applied. The particle stack and angular priors were then transferred to Relion for two rounds of Bayesian polishing. The particle stack was then subjected to no-image alignment 3D classification ($k = 4$/tau_fudge = 20). A total of 82,592 particles contributed to the highest resolution class, and these particles were subjected to another round of Bayesian polishing. The shiny particles were reimported into cryoSPARC for a final round of non-uniform refinement and local refinement with C3 symmetry applied, resulting in a 2.69-Å final reported resolution (FSC = 0.143).

Ribavirin. In total, 3,937 movies were subjected to MotionCorr2 in Relion[52] and CTFFIND4 in cryoSPARC[53]. Micrographs exhibiting a CTF estimated resolution under 6 Å were selected and subjected to template picking in cryoSPARC. After manual curation of pick locations, particles were extracted with a box size of 64 pixels with 4× Fourier binning (4.32 Å per pixel). A total of 2.7 million extracted particles were subjected to 2D classification. Two-dimensional classes featuring strong protein features were then re-extracted with a box size of 256 pixels and no binning (1.08 Å per pixel), followed by a non-uniform refinement with C3 symmetry applied. Two rounds of heterogenous refinements were then performed (both $k = 3$, with C3 applied).The 247,980 particles from the highest resolution class were then subjected to non-uniform refinement with C3 applied and transferred to Relion for two rounds of Bayesian polishing. The shiny particles were reimported into cryoSPARC for a final round of non-uniform refinement with C3 symmetry applied, resulting in a 2.54-Å final reported resolution (FSC = 0.143).

GS4 (consensus). In total, 12,707 movies were subjected to MotionCorr2 in Relion[52] and Gctf in Relion. Micrographs featuring a rlnFigureOfMerit of >0.07 were selected and subjected to template picking in Relion. Particles were extracted with a box size of 64 pixels with 4× Fourier binning (4.32 Å per pixel). A total of 3.6 million extracted particles were subjected to two rounds of 2D classification. Two-dimensional classes featuring strong protein features were then re-extracted with a box size of 256 pixels and no binning (1.08 Å per pixel). The stack of 993,579 particles was imported to cryoSPARC, split by optics group and subjected to non-uniform refinement (C3 applied) with both local and global CTF refinement enabled. The particles were then subjected to two rounds of heterogenous refinements ($k = 6$ then $k = 3$, C3 applied). The resulting 498,109 particles were then subjected to non-uniform refinement (C3), transferred to Relion for one round of Bayesian polishing and reimported to cryoSPARC for a final round of non-uniform refinement (C3, local + global CTF refinement enabled) followed by a local refinement for a final resolution of 2.31 Å (FSC = 0.143).

GS4 (subset). A particle stack of 993,579 identified from early processing on the GS4 dataset (see above) was subjected to one round of heterogenous refinement in cryoSPARC ($k = 4$, C3 applied). In total, 556,379 particles corresponding to the highest resolution class were subjected to non-uniform refinement (C3) and transferred to Relion for Bayesian polishing. The polished particles were then symmetry expanded (C3 operator) with the relion_particle_symmety_expand tool in Relion, leading to a total of 1.7 million expanded particles. A local angular search was then performed with a single protomer masked, followed by signal subtraction. Two rounds of no-image alignment classification were then performed with the protomer mask ($k = 3$/tau_fudge = 20, then $k = 3$/tau_fudge = 40), resulting in 290,664 protomer particles in the highest resolution class. The mask was then updated to only cover the transport domain within the protomer, and a no-image alignment classification was run with $k = 5$/tau_fudge = 64. The highest

resolution class consisted of 177,264 protomer particles and also featured some weak signal in the nucleoside binding site. The mask was then updated again to a sphere only covering the nucleoside binding site. A no-image alignment using this mask was performed with $k = 3$/tau_fudge = 128. The extremely high tau_fudge value was necessary to sort for high-frequency signal in the binding cavity and allowed us to identify a small subset of particles that featured much stronger signal consistent with the size and shape of purine nucleoside. The particles corresponding to this presumably higher-occupancy GS4 class were reverted to the original images and also subjected to remove duplicates to revert symmetry expansion, resulting in 38,774 particles. Angular priors were kept, ensuring that protomers featuring the stronger nucleoside signal remained placed on the same protomeric position within the trimer in angular space. The stack was then transferred to cryoSPARC for a final local refinement (C1 symmetry), with a final reported resolution of 3.23 Å (FSC = 0.143). This subset of 38,774 particles features 1,215 particle overlap (3.1%) with the 498,109 particle 'consensus' set identified in a distinct processing scheme.

MPV condition 1. In total, 4,715 movies were subjected to MotionCorr2 in Relion[52] and CTFFIND4 in cryoSPARC[53]. Micrographs exhibiting a CTF estimated resolution under 4 Å were selected and subjected to template picking in cryoSPARC. After manual curation of pick locations, particles were extracted with a box size of 64 pixels with 4× Fourier binning (4.32 Å per pixel). A total of 2.6 million extracted particles were subjected to 2D classification. Two-dimensional classes featuring strong protein features were then re-extracted with a box size of 128 pixels and 2× binning (2.16 Å per pixel), followed by heterogenous refinement ($k = 3$, C3 applied). The 439,382 particles corresponding to the highest resolution class were then subjected to non-uniform refinement with C3 applied. The particle stack was then transferred to Relion and subjected to two rounds of Bayesian polishing. After reimporting to cryoSPARC, non-uniform refinement was performed with C3 symmetry applied, resulting in a 2.80-Å resolution (FSC = 0.143) consensus reconstruction.

For 3D variability analysis in cryoSPARC, the 439,382 shiny particles in Relion were subjected to an autorefine run in C1 symmetry, with relaxation to C3 enabled. This resulted in a single protomer featuring very weak signal in the transport domain. This C1 reconstruction was then subjected to Bayesian polishing and transferred to cryoSPARC, where it was then subjected to 3D variability analysis, with the protomer featuring weak signal masked (two components, C1, 5 Å low-pass filter, 20 Å high-pass filter, clustering output, $k = 5$). Volumes from the clustering output were apparent 2:1 heterotrimers composed of two INT1 protomers and INT1, INT3 or OFS conformers at the protomeric position that was masked. These volumes were used as references for rounds of heterogenous refinements to obtain a high-quality INT1–INT1–OFS heterotrimer reconstruction (three rounds, $k = 4$, with one OFS–INT1–INT1 reference, one INT3–INT1–INT1 reference and two INT1 homotrimer references as decoys). This classification approach resulted in 118,113 particles that yielded a high-quality OFS–INT1–INT1 reconstruction, with a final reported resolution of 3.20 Å.

MPV condition 2. In total, 3,735 movies were subjected to MotionCorr2 in Relion[52] and CTFFIND4 in cryoSPARC[53]. Micrographs exhibiting a CTF estimated resolution under 6 Å were selected and subjected to template picking in cryoSPARC. After manual curation of pick locations, particles were extracted with a box size of 64 pixels with 4× Fourier binning (4.32 Å per pixel). A total of 2.0 million extracted particles were subjected to two rounds of 2D classification. Two-dimensional classes featuring strong protein features were then re-extracted with a box size of 256 pixels and no binning (1.08 Å per pixel), followed by a non-uniform refinement with C3 symmetry applied. Heterogenous refinement was then performed ($k = 3$, with C3 applied). The 108,187 particles from the highest resolution class were then subjected to non-uniform refinement with C3 applied and transferred to Relion for two rounds of Bayesian polishing. The shiny particles were reimported into cryoSPARC for a final round of non-uniform refinement with C3 symmetry applied, resulting in a 2.99-Å final reported resolution (FSC = 0.143) for the consensus reconstruction.

Cryo-electron microscopy data processing: ensemble analysis

MPV condition 1. The 439,382 shiny particles in Relion (consensus set), immediately after autorefine with C3 applied, were symmetry expanded (C3 operator) with the relion_particle_symmety_expand tool in Relion, leading to a total of 1.3 million expanded particles. Signal subtraction was then performed with a single protomer mask, followed by one round of no-image alignment classification ($k = 6$/tau_fudge = 40). The resulting classes were assigned by conformational state, resulting in 866,559 protomer particles adopting an INT1 state and 250,956 protomer particles adopting an INT3 state. One class, with 199,959 protomer particles, featured extremely weak signal in the transport domain. Based on the 3D variability result from this particle set, we presumed that this class represents the OFS, and the weak signal was resultant from inaccurate angular assignment for trimers containing the OFS conformer into the initial consensus reconstruction.

Having assigned three distinct conformers within the asymmetric unit of bCNT3 in this condition, there are a total of 11 possible arrangements of these three conformers within a bCNT3 trimer: OFS–OFS–OFS, OFS–OFS–INT1, OFS–OFS–INT3, INT1–INT1–OFS, INT1–INT1–INT1, INT1–INT1–INT3, INT3–INT3–OFS, INT3–INT3–INT1, INT3–INT3–INT3, OFS–INT1–INT3 (clockwise) and OFS–INT1–INT3 (counterclockwise). We were then interested in identifying intersecting instances of conformers on grids to obtain cryo-EM reconstructions for every possible trimeric arrangement. Using the Remove Duplicates tool in cryoSPARC (with a minimum separation distance set to 0 Å), we were able to find x/y positions on the grid corresponding to each of these trimeric arrangements. Whereas obtaining reconstructions of the homotrimers was straightforward, obtaining reconstructions of heterotrimers was less straightforward. We noticed that the subtle asymmetric features identified from symmetry expansion often get flattened when subjecting isolated heterotrimer particles to C1 refinements with global angular searches. To keep overlap of assigned conformers at each position of the trimer, angular priors have to be selectively kept from a particular conformer of interest. For example, in a INT1–INT1–INT3 heterotrimer, the INT3 protomer features an INT1 neighbor at both of its flanking trimeric positions. Therefore, selectively keeping priors from the INT3 subset metadata ensures overlap of each assigned conformer in the trimer in angular space. To achieve this, we used the 'Score field' function in the cryoSPARC Remove Duplicates tool (set to 'alignments3D/error') and edited the _rlnMaxValueProbDistribution column to an arbitrary high value (arbitrary low estimated error) for a particular conformer particle subset. This forced the Remove Duplicates tool to drop protomer metadata of the conformer of interest into the 'rejected' stack, which ensured that priors were retained from the conformer of interest for subsequent refinements. For INT1–INT1–INT3, metadata for the protomer particle subset INT1 were edited to contain high_rlnMaxValueProbDistribution values, which forced the priors from INT3 into the 'rejected' stack after using Remove Duplicates to find x/y pick instances of INT1–INT1–INT3 on the grid. For the OFS–INT1–INT3 heteromer, selectively retaining priors from INT1 was insufficient to ensure overlap in conformers in the trimer, as the three conformations could be arranged in two possible directions in the trimer (clockwise or counterclockwise). To break ambiguity in this case, we selectively retained priors from INT1 and performed an additional round of classification in Relion using a mask that covered the INT1 protomer and one of the neighboring protomers ($k = 2$/tau_fudge = 40).

Having identified x/y pick instances for all possible trimer combinations and selectively retaining angular priors during the process

to ensure proper overlap of conformers in the trimer, particles were re-extracted in cryoSPARC and subjected to masked local refinements with C1 applied (for heterotrimer compositions) or C3 applied (in cases of homotrimer compositions). For reconstructions reaching higher resolutions after the first round of local refinement, rounds of Bayesian polishing and CTF refinements were repeated to further improve the final resolution. The 11 obtained reconstructions range in resolution from 3.00 to 6.92 Å (FSC = 0.143), with the lowest-resolution reconstructions suffering from low signal to noise owing to extremely low particle numbers.

MPV condition 2. The 108,187 shiny particles in Relion (consensus set), immediately after autorefine with C3 applied, were symmetry expanded (C3 operator) with the relion_particle_symmety_expand tool in Relion, resolution in a total of 324,561 expanded particles. Signal subtraction was then performed with a single protomer mask, followed by one round of no-image alignment classification (k = 4/tau_fudge = 40). The resulting classes were assigned by conformational state, resulting in 108,297 protomer particles adopting an INT1 state and 102,783 protomer particles adopting an INT2 state. We then applied the aforementioned method (see MPV condition 1) to identify the following trimeric compositions on the grid and obtain reconstructions for each case: INT1–INT1–INT1, INT1–INT1–INT2, INT1–INT2–INT2 and INT2–INT2–INT2. The four reconstructions range in resolution from 3.43 to 3.67 Å (FSC = 0.143).

Model building and refinement

A model was initially built into a preliminary IFS bCNT3 reconstruction via manually docking a polyalanine model of the *Vibrio cholerae* CNT crystal structure (Protein Data Bank (PDB) ID 3TIJ) into the cryo-EM maps, followed by manual model building and adjustments in COOT[55]. Hydrogens were added to the model using the Molprobity server[56], followed by a round of real-space refinement in Phenix[54] with local grid search, global minimization and ADP refinement enabled. This initial model was rigid body fit in all six IFS bCNT3 structures, followed by further minor model adjustments as necessary, drug modeling when relevant and subsequent real-space refinements in Phenix (one round with global minimization and ADP refinement enabled). Lipids were built as fragments of phosphatidylcholine (chemical ID LBN) owing to its abundance in the nanodiscs. Sodium ions and ion coordinating water molecules were modeled in the highest-resolution reconstruction (GS4 consensus). The first site was modeled based on the clear cryo-EM density and precedence[20]. There was ambiguity in ion and water placement in the second sodium site, which was ultimately broken by checking both possibilities with the CMM server[38]. Sodium ions were also placed into other high-resolution reconstructions in cases where the map contained clear ion density.

For OFS, INT1, INT2 and INT3 conformers, an IFS protomer model was initially placed in the cryo-EM maps, followed by rigid body fitting of the transport domain and mobile elements of the scaffold domain. Rounds of manual model building in COOT and real-space refinement in Phenix were performed. Model building was performed using the INT1 or INT2 homotrimeric (C3) reconstructions obtained from the ensemble analyses, the 'highest-resolution' OFS–INT1–INT1 reconstruction (obtained from 3D variability and heterogenous refinement) for the OFS and the INT1–INT1–INT3 reconstruction from condition 1 ensemble analysis for the INT3 conformer. A summary of deposited coordinates can be found in Extended Data Figs. 2, 6 and 7.

Model-to-map correlation analysis of cryo-electron microscopy ensembles

Refined coordinates from the highest-resolution instance of each distinct protomer conformation were used as references for this analysis: the OFS protomer from OFS–INT1–INT1 (highest resolution, MPV dataset 1, 3D variability), INT1 protomer from INT1–INT1–INT1 (ensemble analysis, MPV dataset 1), INT2 protomer from INT1–INT1–INT2 (ensemble analysis, MPV dataset 2) and INT3 protomer from INT1–INT1–INT3 (ensemble analysis, MPV dataset 1). The reference models were trimmed to Cα, and residues 90–200 were removed (eukaryotic scaffold domain). All of the following steps were performed in UCSF Chimera[57]. Conserved scaffold domain elements TM3 and TM6 (trimer) were rigid body fit into each of the reconstructions (unsharpened maps used). Reference protomers were then superposed to the placed scaffold domain at each protomeric position with mmaker. Placed reference protomers were then converted to maps with molmap (output filtered to a resolution of 6 Å). Map correlation coefficients were then calculated between the experimental map and the placed reference volumes for each conformational state.

Molecular dynamics simulation set up and protocol

All all-atom simulation systems and inputs were generated using CHARMM-GUI Membrane Builder[58]. Additionally, SMD systems and inputs were created using CHARMM-GUI Enhanced Sampler[59]. System information, including membrane composition, the total number of atoms and ions and simulation time length, are shown in Supplementary Tables 3 and 4. The CHARMM36(m) force field, TIP3P model and CGenFF were used in each system for protein/lipids[60], water and ligands, respectively. The SHAKE algorithm was used to constrain bond lengths involving hydrogen, and the hydrogen mass repartitioning technique was used to facilitate simulations with a 4-fs time step. van der Waals interactions were handled with a cutoff distance of 12 Å and a force switch between 10 and 12 Å. The particle-mesh Ewald method was used for electrostatic interactions. The NPT ensemble (constant particle number, pressure and temperature) was applied in each system at a pressure of 10^5 Pa and temperature of 310 K, following the default CHARMM-GUI six-step equilibration protocol[61] using OpenMM[62].

In standard MD systems, an additional weak positional restraint (0.12 kcal mol^{-1} Å^{-2}) was applied on protein backbone and sodium ions located at the binding site during the first 5 ns of production, followed by another weak restraint (0.06 kcal mol^{-1} Å^{-2}) during the next 5 ns. After 10 ns, the production continued with no restraints. In SMD systems, dihedral restraints (4.78 kcal mol^{-1} Å^{-2}) were applied on the TM6 helix of the OFS conformer throughout production to maintain its secondary structure. The backbone center of mass of the OFS transport domain was used as the collective variable with a spring constant of 47.8 kcal mol^{-1} Å^{-2} and was pulled down relative to the backbone center of mass of the IFS scaffold domain at a speed of 1 Å ns^{-1} on the $-z$ direction over a total translocation distance of 9 Å. The membrane normal is the z direction, and the $+z$ is the extracellular side. Due to the high energy barrier between the OFS and INT1 conformations, the actual pulling speed was lower, and thus the SMD production continued to 15 ns.

Root mean squared deviation calculations

All r.m.s.d. results from our MD simulations were calculated on heavy atoms of either ligands or the bCNT3 nucleoside binding pocket backbone. In standard MD systems, the bCNT3 snapshots were superimposed by aligning the binding pocket backbone atoms to the initial coordinates to calculate ligand r.m.s.d. In SMD systems, the bCNT3 snapshots were superimposed by aligning the TM3 backbone atoms to the OFS or INT1 coordinates to calculate both the ligand r.m.s.d. and the nucleoside binding pocket r.m.s.d.

Reporting summary

Further information on research design is available in the Nature Portfolio Reporting Summary linked to this article.

Data availability

Atomic coordinates have been deposited in the PDB with the following ID numbers: 8TZ2 (apo), 8TZ5 (NHC), 8TZ6 (PSI-6206), 8TZ1 (ribavirin),

8TZ3 (GS4 consensus), 8TZ4 (GS4 subset), 8TZD (INT1–INT1–OFS; MPV condition 1), 8TZ7 (INT1 homotrimer; MPV condition 1 ensemble), 8TZ8 (INT1–INT1–INT3; MPV condition 1 ensemble), 8TZA (INT1–INT1–INT2; MPV condition 2 ensemble) and 8TZ9 (INT2 homotrimer; MPV condition 2 ensemble). The reconstructed cryo-EM maps have been deposited in the Electron Microscopy Data Bank with the following ID numbers: EMD-41731 (apo), EMD-41734 (NHC), EMD-41735 (PSI-6206), EMD-41730 (ribavirin), EMD-41732 (GS4 consensus), EMD-41733 (GS4 subset), EMD-41755 (INT1–INT1–OFS; MPV condition 1), EMD-41736 (INT1 homotrimer; MPV condition 1 ensemble), EMD-41737 (INT1–INT1–INT3; MPV condition 1 ensemble), EMD-41738 (INT2 homotrimer; MPV condition 2 ensemble), EMD-41739 (INT1–INT1–INT2; MPV condition 2 ensemble), EMD-41740 (consensus; MPV condition 1), EMD-41752 (consensus; MPV condition 2), EMD-41747 (INT3 homotrimer; MPV condition 1 ensemble), EMD-41746 (INT3–INT3–INT1; MPV condition 1 ensemble), EMD-41745 (INT3–INT3–OFS; MPV condition 1 ensemble), EMD-41744 (INT1–INT1–OFS; MPV condition 1 ensemble), EMD-41741 (OFS–OFS–OFS; MPV condition 1 ensemble), EMD-41742 (OFS–OFS–INT1; MPV condition 1 ensemble), EMD-41743 (OFS–OFS–INT3; MPV condition 1 ensemble), EMD-41748 (OFS–INT1–INT3 clockwise; MPV condition 1 ensemble), EMD-41749 (OFS–INT1–INT3 counterclockwise; MPV condition 1 ensemble), EMD-41751 (INT1 homotrimer; MPV condition 2 ensemble) and EMD-41750 (INT1–INT2–INT2; MPV condition 2 ensemble). Source data are provided with this paper. Additional data relevant to this paper are available upon reasonable request to S.-Y. L.

References

51. Wright, N. J. et al. Methotrexate recognition by the human reduced folate carrier SLC19A1. *Nature* **609**, 1056–1062 (2022).
52. Kimanius, D., Dong, L., Sharov, G., Nakane, T. & Scheres, S. H. W. New tools for automated cryo-EM single-particle analysis in RELION-4.0. *Biochem. J.* **478**, 4169–4185 (2021).
53. Punjani, A., Rubinstein, J. L., Fleet, D. J. & Brubaker, M. A. cryoSPARC: algorithms for rapid unsupervised cryo-EM structure determination. *Nat. Methods* **14**, 290–296 (2017).
54. Liebschner, D. et al. Macromolecular structure determination using X-rays, neutrons and electrons: recent developments in Phenix. *Acta Crystallogr. D Struct. Biol.* **75**, 861–877 (2019).
55. Emsley, P. & Cowtan, K. Coot: model-building tools for molecular graphics. *Acta Crystallogr. D Biol. Crystallogr.* **60**, 2126–2132 (2004).
56. Williams, C. J. et al. MolProbity: More and better reference data for improved all-atom structure validation. *Protein Sci.* **27**, 293–315 (2018).
57. Pettersen, E. F. et al. UCSF ChimeraX: structure visualization for researchers, educators, and developers. *Protein Sci.* **30**, 70–82 (2021).
58. Wu, E. L. et al. CHARMM—GUI membrane builder toward realistic biological membrane simulations. *J. Comput. Chem.* **35**, 1997–2004 (2014).
59. Suh, D. et al. CHARMM—GUI enhanced sampler for various collective variables and enhanced sampling methods. *Protein Sci.* **31**, e4446 (2022).
60. Huang, J. et al. CHARMM36m: an improved force field for folded and intrinsically disordered proteins. *Nat. Methods* **14**, 71–73 (2017).
61. Jo, S., Kim, T. & Im, W. Automated builder and database of protein/membrane complexes for molecular dynamics simulations. *PLoS ONE* **2**, e880 (2007).
62. Eastman, P. et al. OpenMM 7: rapid development of high performance algorithms for molecular dynamics. *PLoS Comput. Biol.* **13**, e1005659 (2017).

Acknowledgements

Cryo-EM data were screened and collected at the Duke University SMIF, the National Cancer Institute's NCEF at the Frederick National Laboratory for Cancer Research, the Pacific Northwest Center for Cryo-EM (PNCC) at Oregon Health and Science University and the National Institute of Environmental Health Sciences. We thank J. Myers at PNCC, A. Wier, T. Fox and U. Baxa at NCEF and N. Bhattacharya at SMIF for assistance with microscope operation. We thank M. Hirschi for initial biochemistry of bCNT3 and K. Tsolova for help with part of the radioactive tracer uptake assay and manuscript reading. This research was supported by a National Institutes of Health grant R21AI166134 (S.-Y.L.) and the National Institute of Health Intramural Research Program, the US National Institutes of Environmental Health Science (ZIC ES103326 to M.J.B.) and the National Science Foundation (MCB-2111728 to W.I.). A portion of this research was supported by National Institutes of Health grant U24GM129547, was performed at the PNCC at Oregon Health and Science University and was accessed through EMSL (grid.436923.9), a Department of Energy Office of Science User Facility sponsored by the Office of Biological and Environmental Research. The Duke University SMIF is affiliated with the North Carolina Research Triangle Nanotechnology Network, which is, in part, supported by the National Science Foundation (ECCS-2025064).

Author contributions

N.J.W. conducted biochemical preparation, sample freezing, single-particle 3D reconstruction, model building and radiotracer uptake assays. F.Z. performed electrophysiological recordings. Y.S. collected data and performed part of structural analysis. Y.Y. performed biochemical characterization of bCNT3, and J.F. performed part of the radiotracer uptake assay, all under the guidance of S.-Y.L. L.K. performed all MD simulations under the guidance of W.I. K.S. performed part of the cryo-EM sample screening under the guidance of M.J.B. N.J.W. and S.-Y.L. wrote the paper with input from the rest of authors.

Competing interests

The authors declare no competing interests.

Additional information

Extended data is available for this paper at https://doi.org/10.1038/s41589-024-01559-8.

Supplementary information The online version contains supplementary material available at https://doi.org/10.1038/s41589-024-01559-8.

Correspondence and requests for materials should be addressed to Seok-Yong Lee.

Peer review information *Nature Chemical Biology* thanks Raimund Dutzler and the other, anonymous, reviewers for their contribution to the peer review of this work.

https://doi.org/10.1038/s41589-024-01559-8

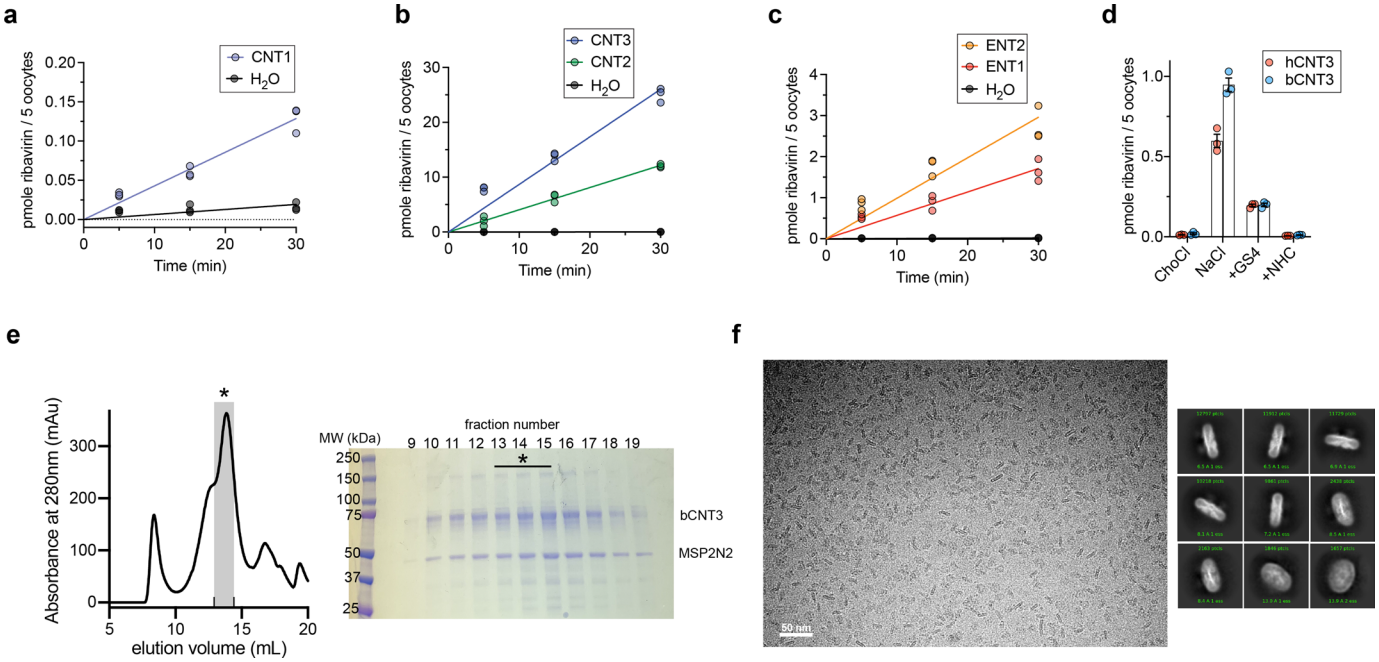

Extended Data Fig. 1 | Functional characterization, protein biochemistry, and cryo-EM sample preparation of bCNT3. a, b, c, Time-dependent uptake of 1.0 µM [^{3}H]-ribavirin at room temperature is linear within 30 min for hCNT1 (**a**, background corrected uptake rate of 0.0036 ± 0.0002 pmole/min), hCNT2 (**b**, background corrected uptake rate of 0.41 ± 0.01 pmole/min), hCNT3 (**b**, background corrected uptake rate of 0.87 ± 0.04 pmole/min), hENT1 (**c**, background corrected uptake rate of 0.056 ± 0.004 pmole/min) and hENT2 (**c**, background corrected uptake rate of 0.098 ± 0.007 pmole/min). Data shown in panels **a**, **b**, **c** are from the same series of experiments (n = 3 biological replicates, individual replicates shown) with the water-injected control measurements re-shown in each figure panel to convey signal-to-background for each transporter subtype. **d**, Cold-competition of WT hCNT3 or WT bCNT3 mediated [^{3}H]-ribavirin uptake by cold NHC or GS4. (ChoCl – sodium-free negative control condition with 96 mM choline chloride; 15-minute uptake with 0.1 µM [^{3}H]-ribavirin; n = 3 biological replicates with individual replicates and mean ± s.e.m. shown). **e**, Representative size-exclusion chromatography profile and corresponding SDS-PAGE analysis of purified nanodisc reconstituted bCNT3. Fractions pooled for cryo-EM analysis indicated with an asterisk (*). Purification and nanodisc reconstitution of bCNT3 was repeated routinely with similar results for each cryo-EM structure reported in this study. **f**, Representative cryo-EM micrograph (top) and 2D class averages (bottom) of nanodisc reconstituted bCNT3. Micrographs of similar quality were recorded for each cryo-EM dataset.

https://doi.org/10.1038/s41589-024-01559-8

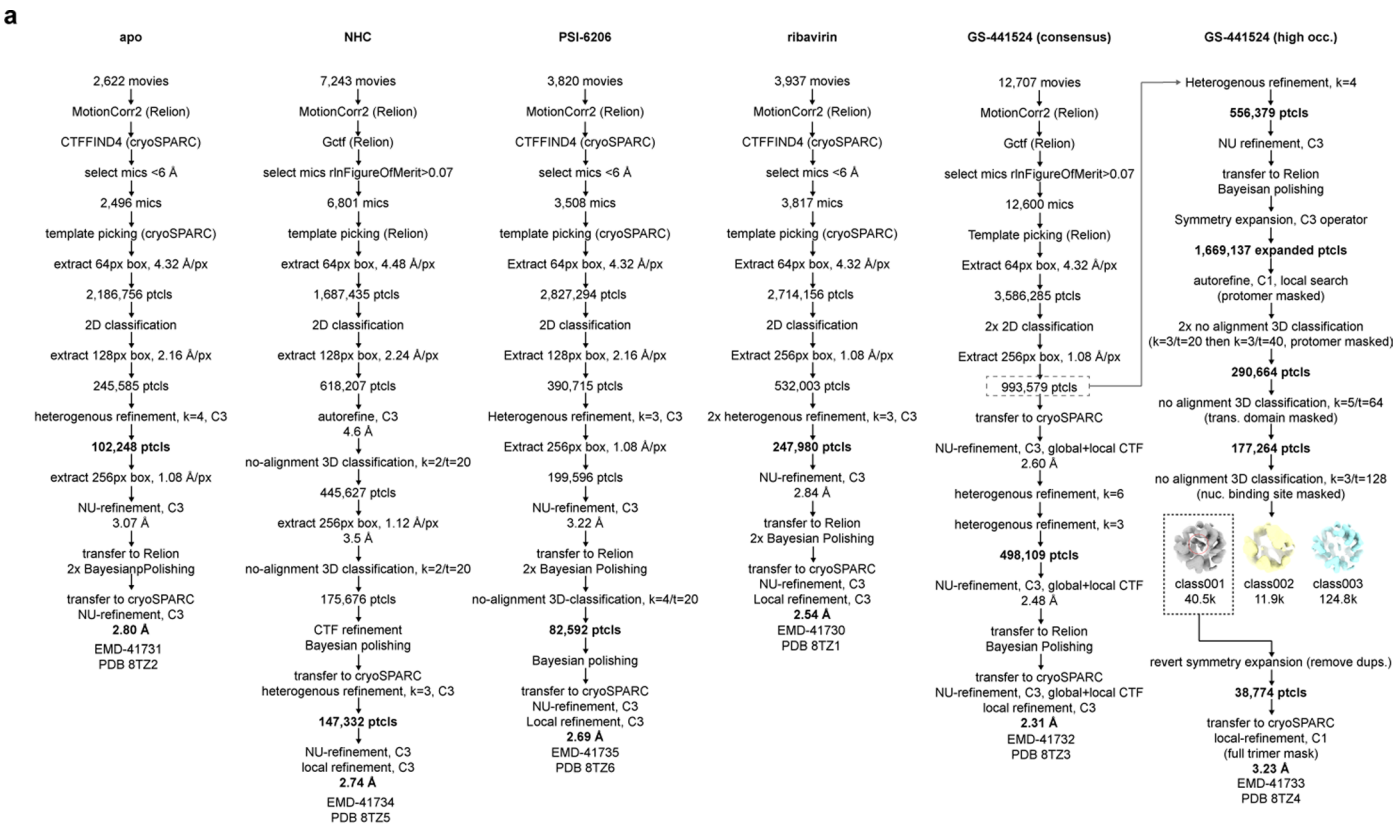

Extended Data Fig. 2 | Cryo-EM image processing of drug-bound and drug-free IFS states of bCNT3. a, Cryo-EM image processing procedures. **b**, Fourier-shell correlation plots (top) and angular orientation distributions (bottom) from the final reconstructions. **c**, Local resolution of the final reconstructions (local resolution determined in cryoSPARC).

https://doi.org/10.1038/s41589-024-01559-8

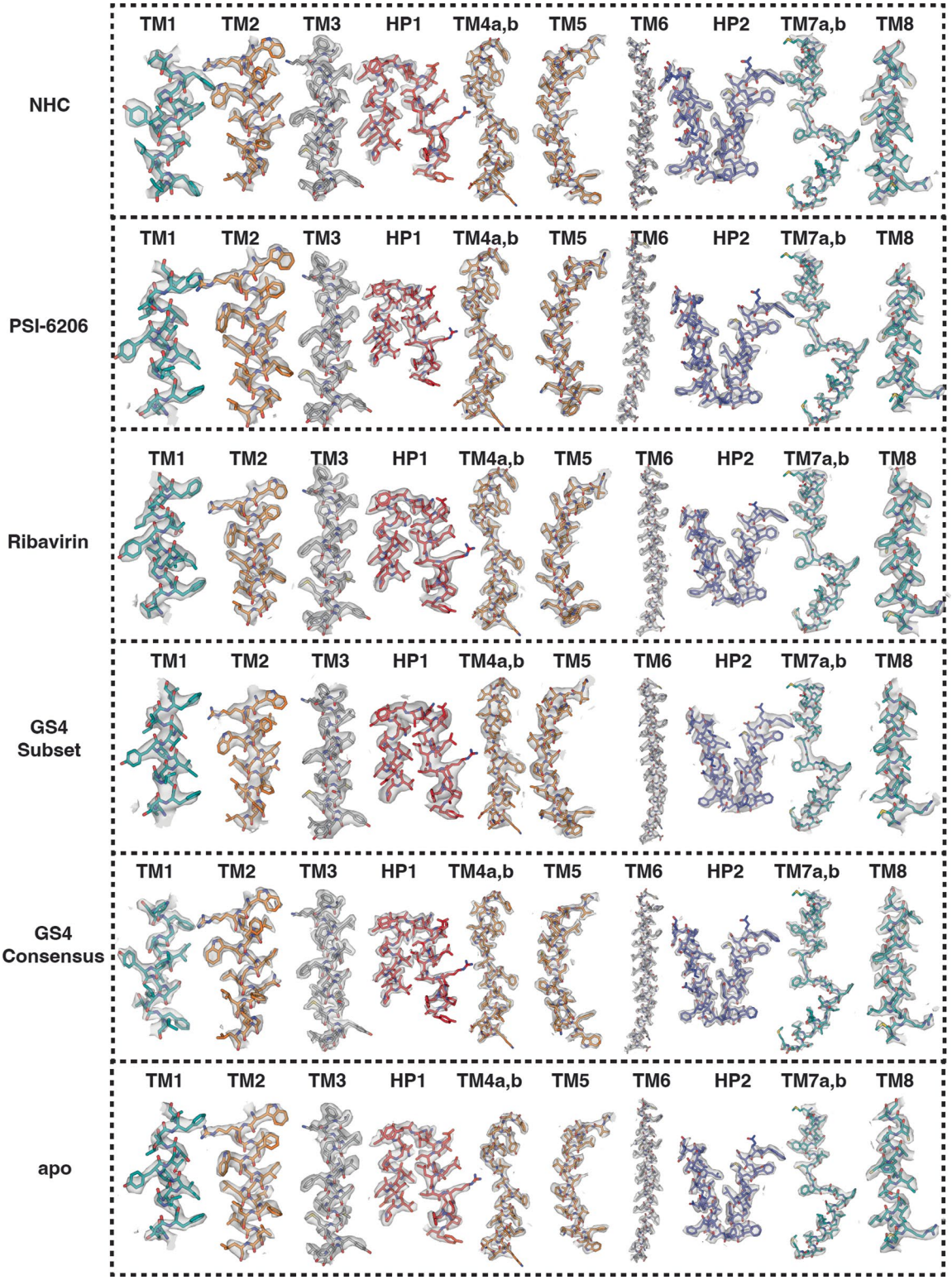

Extended Data Fig. 3 | Local cryo-EM map quality. Local cryo-EM maps for secondary structure segments. From top to bottom are NHC, PSI-6206, Ribavirin, GS441524 (subset), GS441524 (consensus) and apo, respectively. Cryo-EM densities are shown at map threshold values of 6σ for NHC, PSI-6206, ribavirin, GS4 sub., apo, or 7σ for GS4 cons.

https://doi.org/10.1038/s41589-024-01559-8

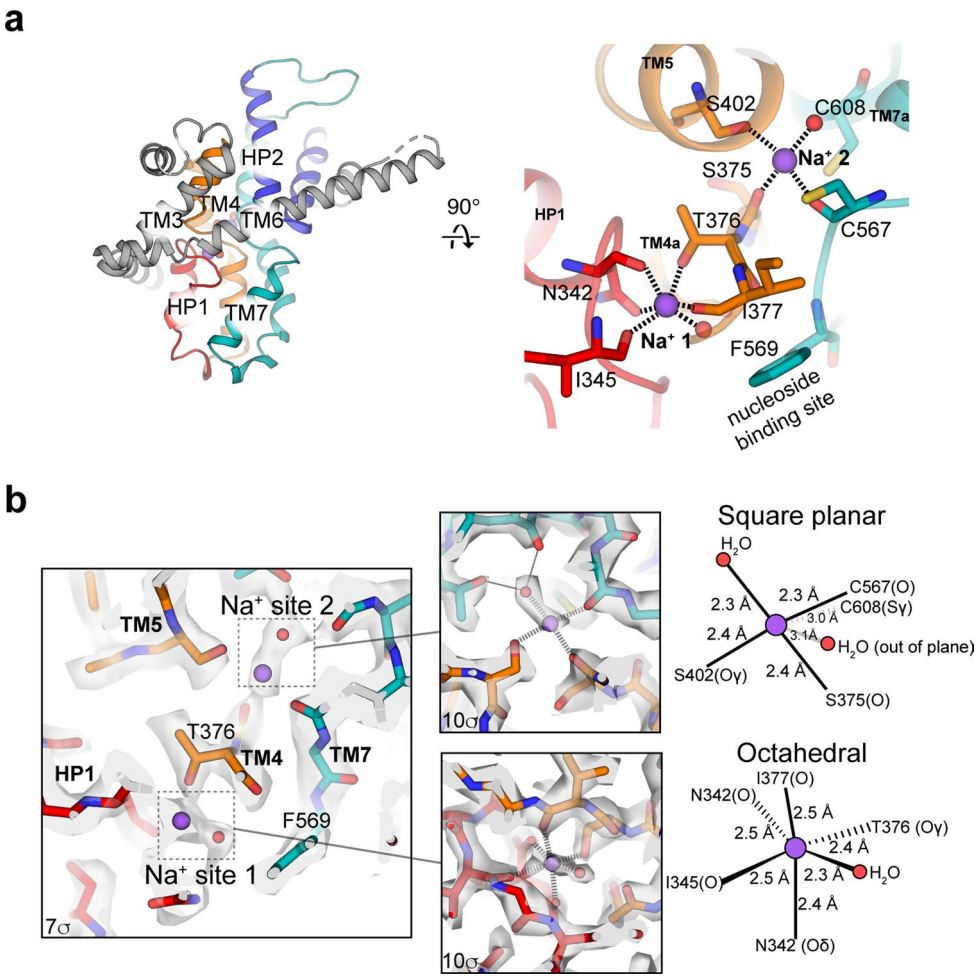

Extended Data Fig. 4 | Sodium ion coordination in the inward-facing state. a, Location of the two sodium ion binding sites relative to the nucleoside binding site within the NHC bound IFS bCNT3 structure. **b**, Architecture and coordination geometries of the two sodium ion binding sites in the 2.31 Å cryo-EM map (map thresholds used denoted in panel insets).

https://doi.org/10.1038/s41589-024-01559-8

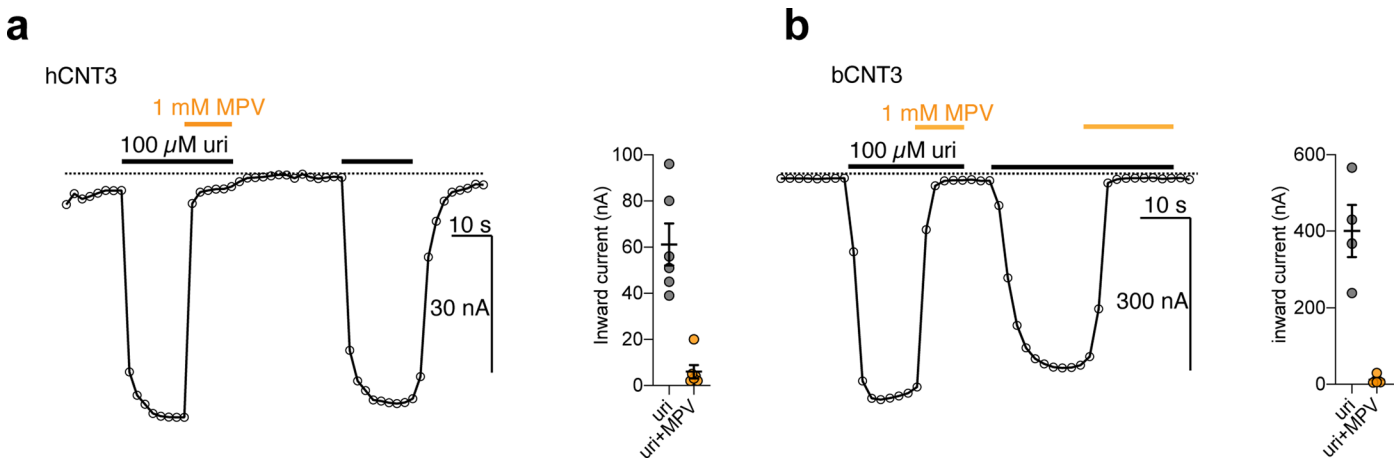

Extended Data Fig. 5 | TEVC studies of molnupiravir interaction with CNT3. **a**, TEVC recordings of inward currents elicited by application of 100 μM uridine, or current block by co-application of 100 μM uridine + 1 mM MPV in WT hCNT3 expressing oocytes (representative trace at left, summary of peak currents from $n = 6$ biological replicates at right with individual measurements and mean ± s.e.m. shown; values are baseline corrected to leak current per oocyte). **b**, TEVC recordings of inward currents elicited by application of 100 μM uridine, or current block by co-application of 100 μM uridine + 1 mM MPV in WT bCNT3 expressing oocytes (representative trace at left, summary of peak currents from $n = 4$ biological replicates at right with individual measurements and mean ± s.e.m. shown; values are baseline corrected to leak current per oocyte).

https://doi.org/10.1038/s41589-024-01559-8

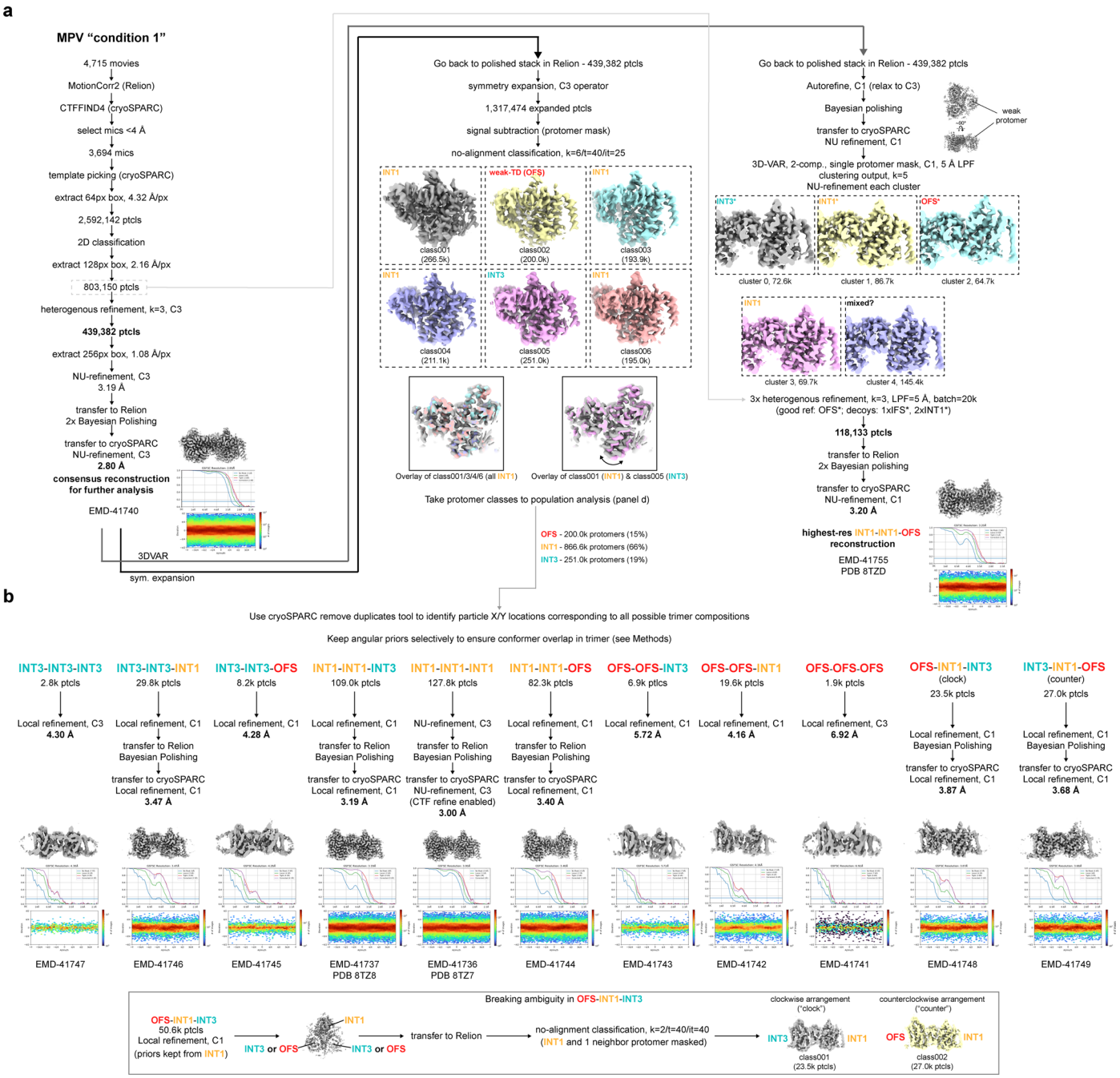

Extended Data Fig. 6 | Cryo-EM image processing of molnupiravir-bound OFS, INT1, INT2, INT3 conformational states of bCNT3. a, Initial cryo-EM image processing procedure for the 'MPV condition 1' dataset. **b**, Cryo-EM ensemble analysis of 'MPV condition 1'. Final Fourier shell correlation plots and angular orientation distribution plots shown next to every reconstruction obtained.

https://doi.org/10.1038/s41589-024-01559-8

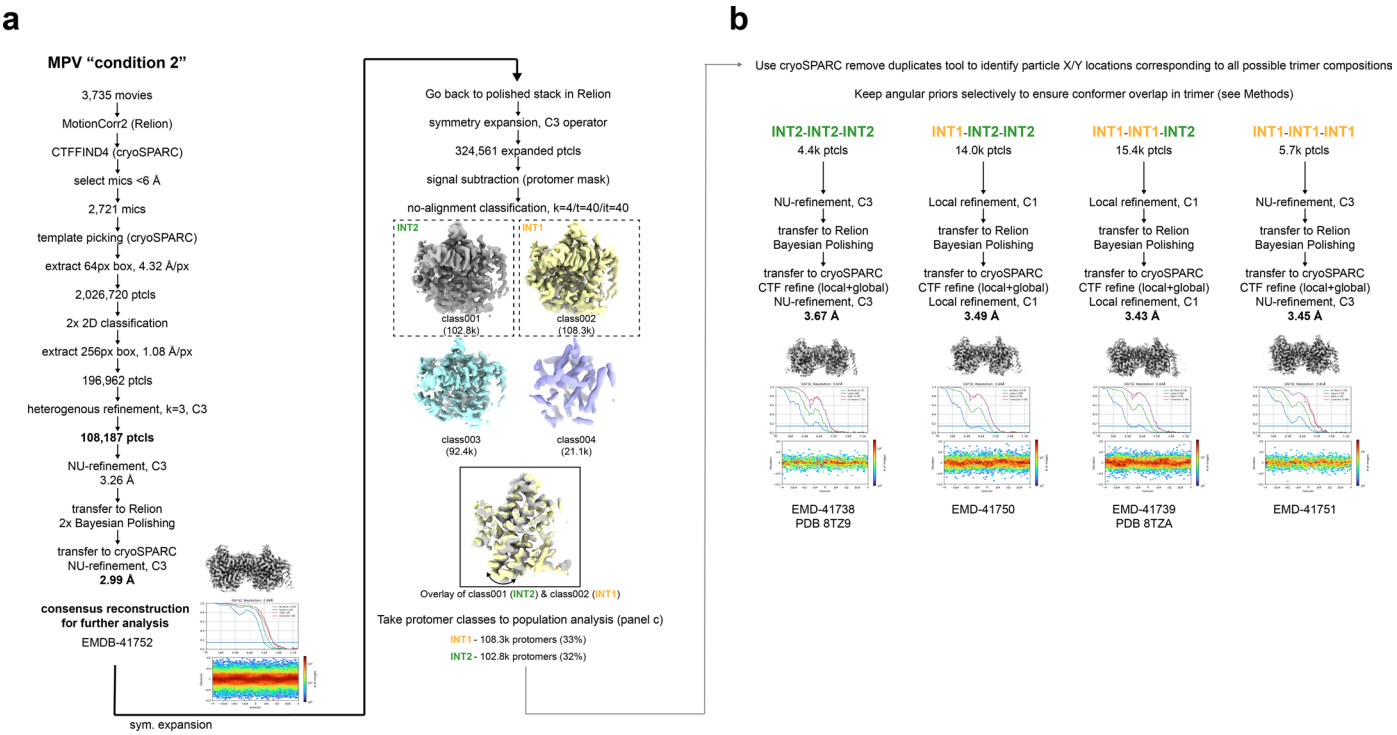

Extended Data Fig. 7 | Cryo-EM image processing of molnupiravir-bound INT1 and INT2 conformational states of bCNT3. a, Initial cryo-EM image processing procedure for the 'MPV condition 2' dataset. **b**, Cryo-EM ensemble analysis of 'MPV condition 2'. Final Fourier shell correlation plots and angular orientation distribution plots shown next to every reconstruction obtained.

https://doi.org/10.1038/s41589-024-01559-8

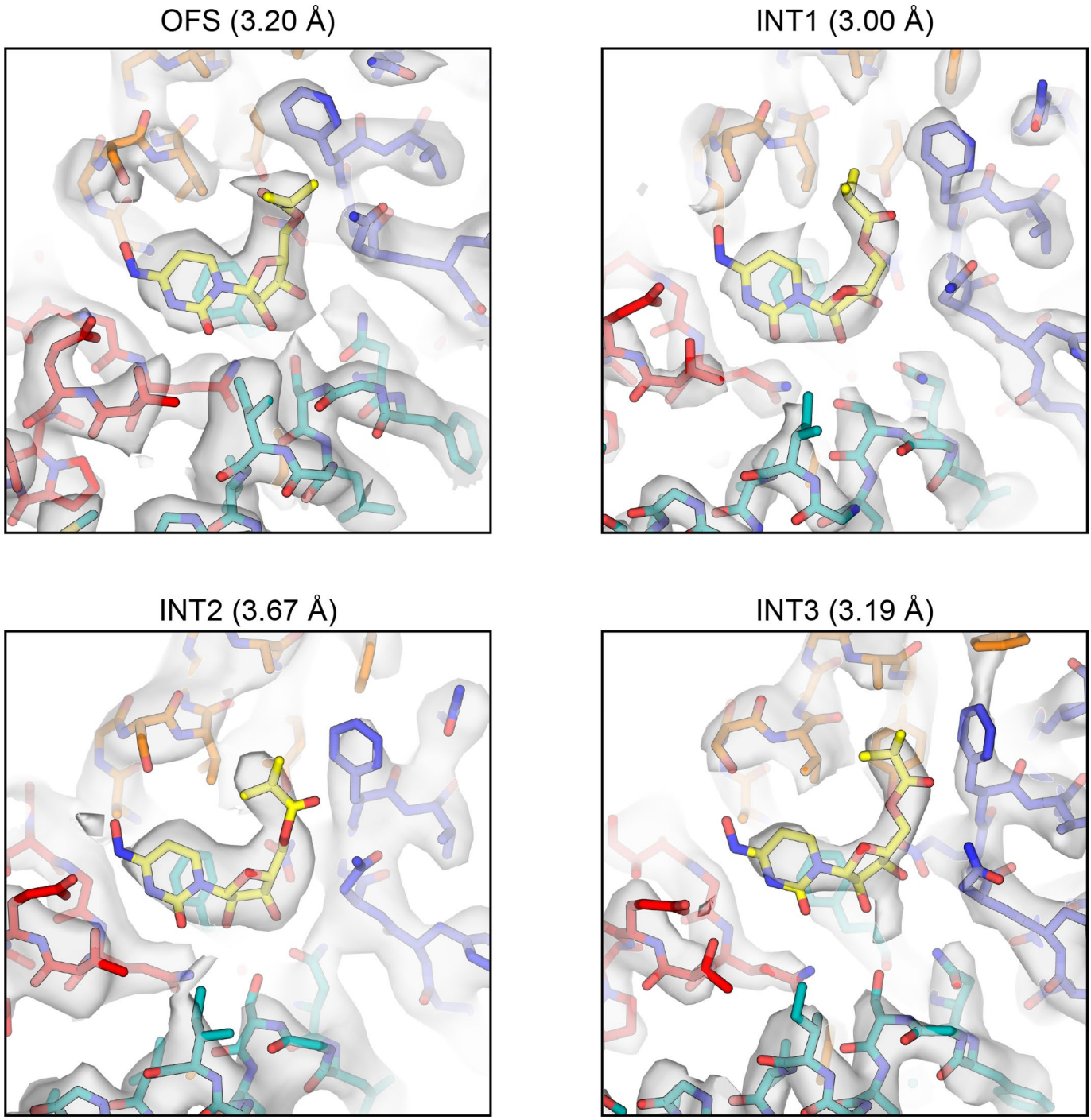

Extended Data Fig. 8 | MPV ligand densities in representative OFS, INT1, INT2, and INT3 cryo-EM reconstructions. Cryo-EM densities around the nucleoside binding site from representative reconstructions containing OFS, INT1, INT2, or INT3 protomers (reconstructions used: OFS-INT1-INT1 highest res; INT1-INT1-INT1 'condition 1' ensemble analysis; INT2-INT2-INT2 'condition 2' ensemble analysis; INT1-INT1-INT3 'condition 1' ensemble analysis). Sharpened maps shown (threshold = 6σ).

https://doi.org/10.1038/s41589-024-01559-8

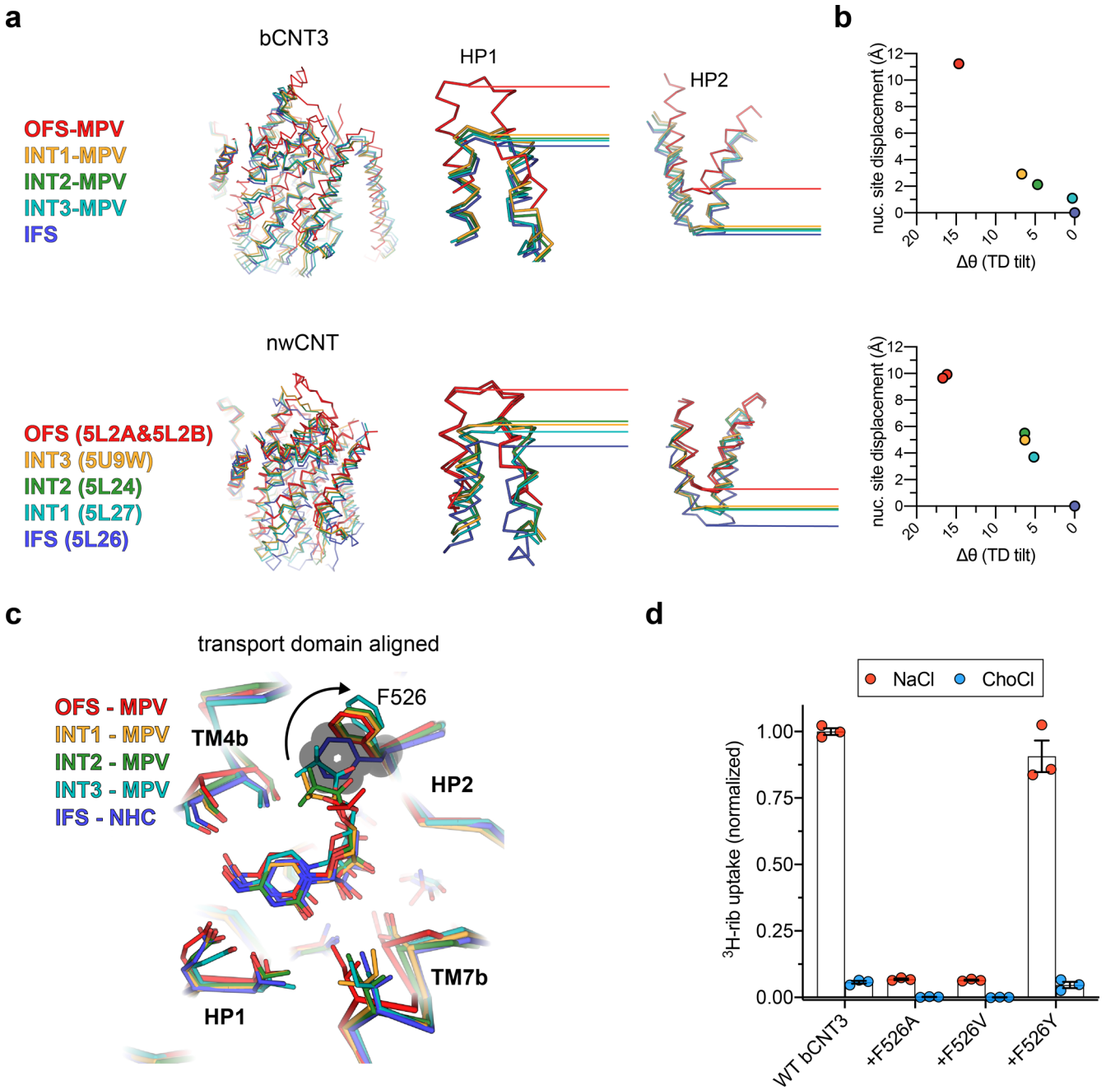

Extended Data Fig. 9 | Comparison of conformational trajectories in MPV-loaded bCNT3 and apo nwCNT. a, Structural superposition of bCNT3 (top left) and nwCNT (bottom left) conformers. Alignment based on the trimerization interface, TM3 and TM6. Relative positions of HP1 (middle) and HP2 (right), with lines denoting a marker residue for each conformational state. **b**, Transport domain movement quantified by its tilt angle relative to a representative IFS structure (X-axis) and distance displacement of nucleoside binding site center of mass (Y-axis). For bCNT3, coordinates corresponding to the highest resolution instance of each conformer used for the analysis (OFS-INT1-INT1 highest res; INT1-INT1-INT1 'condition 1' ensemble analysis; INT2-INT2-INT2 'condition 2' ensemble analysis; INT1-INT1-INT3 'condition 1' ensemble analysis; all relative to the GS4 consensus IFS structure). **c**, Structural superposition of the transport domain for OFS, INT1, INT3, INT3 and IFS (NHC) structures. **d**, [^{3}H]-ribavirin uptake (1.0 μM) in 10 minutes into oocytes expressing WT or mutant bCNT3 ($n = 3$; mean ± s.e.m. and individual replicates shown).

https://doi.org/10.1038/s41589-024-01559-8

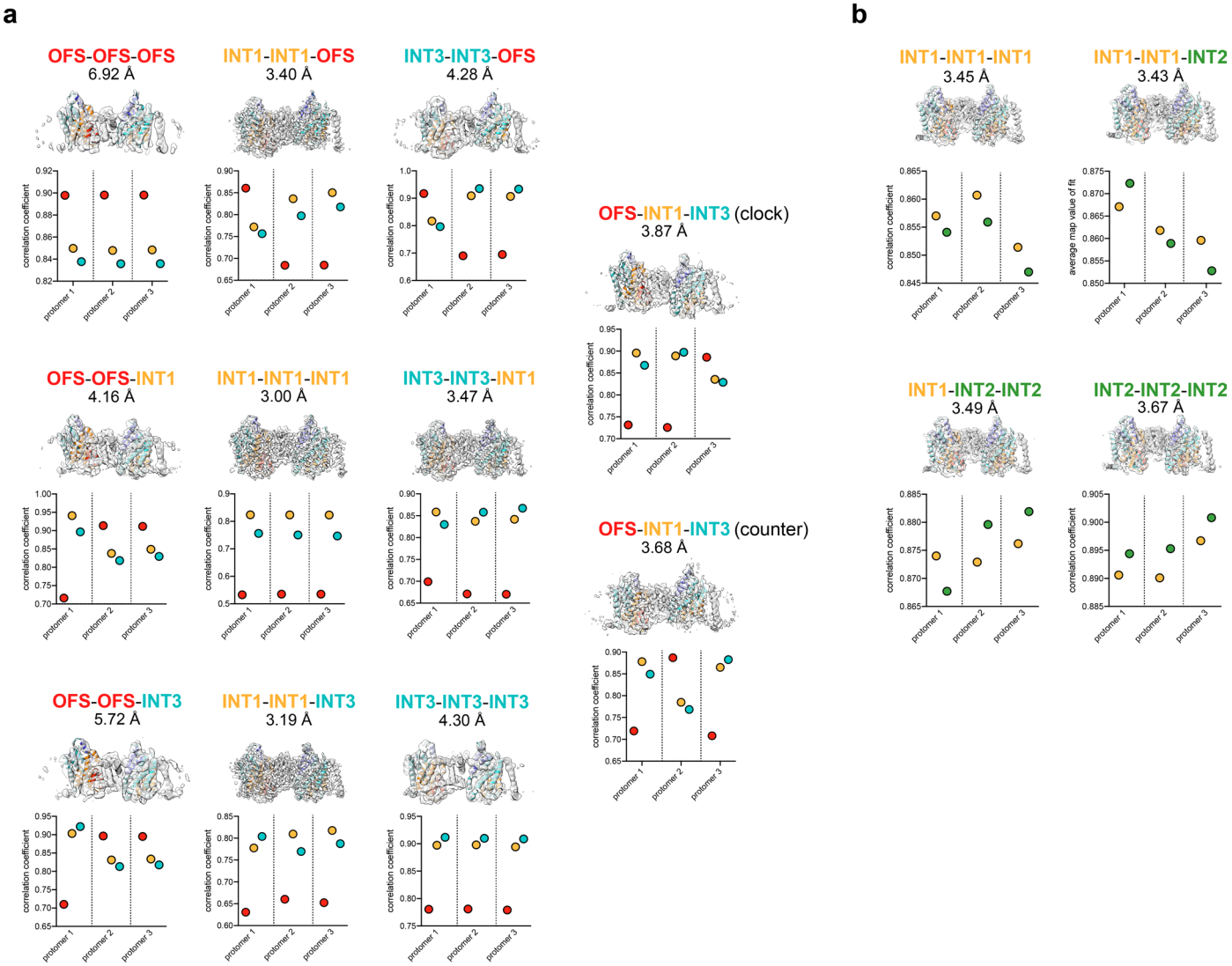

Extended Data Fig. 10 | Map-to-model analysis for reconstructions obtained from the cryo-EM ensemble analysis. a, Map-to-model of every trimer reconstruction obtained from MPV 'condition 1' with the ensemble analysis. Map-to-model correlation analysis shown below each reconstruction (for details see Methods). **b**, Map to model of every trimer reconstruction obtained from MPV 'condition 2' with the ensemble analysis. Map-model correlation analysis shown below each reconstruction (for details see Methods).

nature portfolio

Corresponding author(s): Seok-Yong Lee

Last updated by author(s): 1/6/2024

Reporting Summary

Nature Portfolio wishes to improve the reproducibility of the work that we publish. This form provides structure for consistency and transparency in reporting. For further information on Nature Portfolio policies, see our Editorial Policies and the Editorial Policy Checklist.

Statistics

For all statistical analyses, confirm that the following items are present in the figure legend, table legend, main text, or Methods section.

n/a	Confirmed
☐	☒ The exact sample size (*n*) for each experimental group/condition, given as a discrete number and unit of measurement
☐	☒ A statement on whether measurements were taken from distinct samples or whether the same sample was measured repeatedly
☒	☐ The statistical test(s) used AND whether they are one- or two-sided *Only common tests should be described solely by name; describe more complex techniques in the Methods section.*
☒	☐ A description of all covariates tested
☒	☐ A description of any assumptions or corrections, such as tests of normality and adjustment for multiple comparisons
☐	☒ A full description of the statistical parameters including central tendency (e.g. means) or other basic estimates (e.g. regression coefficient) AND variation (e.g. standard deviation) or associated estimates of uncertainty (e.g. confidence intervals)
☐	☒ For null hypothesis testing, the test statistic (e.g. *F*, *t*, *r*) with confidence intervals, effect sizes, degrees of freedom and *P* value noted *Give P values as exact values whenever suitable.*
☒	☐ For Bayesian analysis, information on the choice of priors and Markov chain Monte Carlo settings
☒	☐ For hierarchical and complex designs, identification of the appropriate level for tests and full reporting of outcomes
☒	☐ Estimates of effect sizes (e.g. Cohen's *d*, Pearson's *r*), indicating how they were calculated

Our web collection on statistics for biologists contains articles on many of the points above.

Software and code

Policy information about availability of computer code

Data collection	Latitude S 1.3 - commercially available, SerialEM 3.8 - published and freely available
Data analysis	MotionCor2 1.2.6 - published and freely available, CTFFIND4 - published and freely available, Relion 3.1/4.0 - published and freely available, UCSF pyem v0.5 - published and open source, CryoSPARC 3.0/3.1 - commercially available, Coot 0.8 - published and freely available, PHENIX 1.18 - published and freely available, UCSF ChimeraX v1.3 - published and freely available, Prism 8 -commercially available, PyMOL 2.4.0 - open source, pClamp 10.6 software - commercially available (Molecular Devices)

For manuscripts utilizing custom algorithms or software that are central to the research but not yet described in published literature, software must be made available to editors and reviewers. We strongly encourage code deposition in a community repository (e.g. GitHub). See the Nature Portfolio guidelines for submitting code & software for further information.

Data

Policy information about availability of data

All manuscripts must include a data availability statement. This statement should provide the following information, where applicable:

- Accession codes, unique identifiers, or web links for publicly available datasets
- A description of any restrictions on data availability
- For clinical datasets or third party data, please ensure that the statement adheres to our policy

Atomic coordinates have been deposited in the Protein Data Bank with the PDB IDs: 8TZ2 (apo), 8TZ5 (NHC), 8TZ6 (PSI-6206), 8TZ1 (ribavirin), 8TZ3 (GS4 cons.),

8TZ4 (GS4 subset), 8TZD (INT1-INT1-OFS;MPV cond. 1), 8TZ7 (INT1 homotrimer; MPV cond. 1 ensemble), 8TZ8 (INT1-INT1-INT3;MPV cond. 1 ensemble), 8TZA (INT1-INT1-INT2;MPV cond. 2 ensemble), 8TZ9 (INT2 homotrimer; MPV cond. 2 ensemble). The reconstructed cryo-EM maps have been deposited in the Electron Microscopy Data Bank with the IDs: EMD-41731 (apo), EMD-41734 (NHC), EMD-41735 (PSI-6206), EMD-41730 (ribavirin), EMD-41732 (GS4 cons.), EMD-41733 (GS4 subset), EMD-41755 (INT1-INT1-OFS;MPV cond. 1), EMD-41736 (INT1 homotrimer; MPV cond. 1 ensemble), EMD-41737 (INT1-INT1-INT3;MPV cond. 1 ensemble), EMD-41738 (INT2 homotrimer; MPV cond. 2 ensemble), EMD-41739 (INT1-INT1-INT2;MPV cond. 2 ensemble), EMD-41740 (consensus; MPV cond. 1), EMD-41752 (consensus; MPV cond. 2), EMD-41747 (INT3 homotrimer; MPV cond. 1 ensemble), EMD-41746 (INT3-INT3-INT1;MPV cond. 1 ensemble), EMD-41745 (INT3-INT3-OFS;MPV cond. 1 ensemble), EMD-41744 (INT1-INT1-OFS;MPV cond. 1 ensemble), EMD-41741 (OFS-OFS-OFS;MPV cond. 1 ensemble), EMD-41742 (OFS-OFS-INT1;MPV cond. 1 ensemble), EMD-41743 (OFS-OFS-INT3;MPV cond. 1 ensemble), EMD-41748 (OFS-INT1-INT3 clockwise; MPV cond. 1 ensemble), EMD-41749 (OFS-INT1-INT3 counterclockwise; MPV cond. 1 ensemble), EMD-41751 (INT1 homotrimer; MPV cond. 2 ensemble), EMD-41750 (INT1-INT2-INT2;MPV cond. 2 ensemble). Source data will be provided with the paper online, and additional data relevant to this paper are available upon reasonable request to S-Y. L.

Research involving human participants, their data, or biological material

Policy information about studies with human participants or human data. See also policy information about sex, gender (identity/presentation), and sexual orientation and race, ethnicity and racism.

Reporting on sex and gender	n/a
Reporting on race, ethnicity, or other socially relevant groupings	n/a
Population characteristics	n/a
Recruitment	n/a
Ethics oversight	n/a

Note that full information on the approval of the study protocol must also be provided in the manuscript.

Field-specific reporting

Please select the one below that is the best fit for your research. If you are not sure, read the appropriate sections before making your selection.

☒ Life sciences ☐ Behavioural & social sciences ☐ Ecological, evolutionary & environmental sciences

For a reference copy of the document with all sections, see nature.com/documents/nr-reporting-summary-flat.pdf

Life sciences study design

All studies must disclose on these points even when the disclosure is negative.

Sample size	The amount of data required for cryo-EM structure determination was determined empirically, with the goal of obtaining the highest resolution structure while considering resource allocation. As bCNT3 is a relatively stable/large target, ~5000 movies were generally sufficient to obtain high-resolution cryo-EM structures. In samples for the oocyte experiments, sample sizes of at least n=3 (biologically independent replicates) were sufficient to ensure reproducibility. For the in vitro assays are presented in this study, which exhibit robust signal to background, predetermination of sample size was not required.
Data exclusions	No data were excluded from functional assays and electrophysiology. Junk particle removal via image classification was performed during cryo-EM data processing, to identify a subset of particle images that led to good 3D-reconstructions.
Replication	At least triplicate ($n \geq 3$) biological repeats were pursued for all functional experiments and were reproducible (sample size is noted in all cases in the figure legends).
Randomization	Randomization was not used for the functional and structural studies reported here because no grouping was needed.
Blinding	Blinding was not used for the functional and structural studies reported here since no grouping was performed.

Reporting for specific materials, systems and methods

We require information from authors about some types of materials, experimental systems and methods used in many studies. Here, indicate whether each material, system or method listed is relevant to your study. If you are not sure if a list item applies to your research, read the appropriate section before selecting a response.

Materials & experimental systems

n/a	Involved in the study
☒	☐ Antibodies
☐	☒ Eukaryotic cell lines
☒	☐ Palaeontology and archaeology
☒	☐ Animals and other organisms
☒	☐ Clinical data
☒	☐ Dual use research of concern
☒	☐ Plants

Methods

n/a	Involved in the study
☒	☐ ChIP-seq
☒	☐ Flow cytometry
☒	☐ MRI-based neuroimaging

Eukaryotic cell lines

Policy information about cell lines and Sex and Gender in Research

Cell line source(s)	Spodoptera frugiperda Sf21 cells (Sf9) were purchased from ATCC, X. laevis oocytes are purchased from Xenopus 1 (Dexter, Michigan, USA)
Authentication	Cell lines were not authenticated.
Mycoplasma contamination	Sf9 cells were not tested for mycoplasma contamination.
Commonly misidentified lines (See ICLAC register)	No commonly misidentified cell line was used in this study.